

An Examination of Version-5 Rainfall Estimates from the TRMM Microwave Imager, Precipitation Radar, and Rain Gauges on Global, Regional, and Storm Scales

STEPHEN W. NESBITT* AND EDWARD J. ZIPSER

Department of Meteorology, University of Utah, Salt Lake City, Utah

CHRISTIAN D. KUMMEROW

Department of Atmospheric Science, Colorado State University, Fort Collins, Colorado

(Manuscript received 7 July 2003, in final form 14 January 2004)

ABSTRACT

An evaluation of the version-5 precipitation radar (PR; algorithm 2A25) and Tropical Rainfall Measuring Mission (TRMM) Microwave Imager (TMI; algorithm 2A12) rainfall products is performed across the Tropics in two ways: 1) by comparing long-term TRMM rainfall products with Global Precipitation Climatology Centre (GPCC) global rain gauge analyses and 2) by comparing the rainfall estimates from the PR and TMI on a rainfall feature-by-feature basis within the narrow swath of the PR using a 1-yr database of classified precipitation features (PFs). The former is done to evaluate the overall biases of the TMI and PR relative to “ground truth” to examine regional differences in the estimates; the latter allows a direct comparison of the estimates with the same sampling area, also identifying relative biases as a function of storm type. This study finds that the TMI overestimates rainfall in most of the deep Tropics and midlatitude warm seasons over land with respect to both the GPCC gauge analysis and the PR (which agrees well with the GPCC gauges in the deep Tropics globally), in agreement with past results. The PR is generally higher than the TMI in midlatitude cold seasons over land areas with gauges. The analysis by feature type reveals that the TMI overestimates relative to the PR are due to overestimates in mesoscale convective systems and in most features with 85-GHz polarization-corrected temperature of less than 250 K (i.e., with a significant optical depth of precipitation ice). The PR tended to be higher in PFs without an ice-scattering signature of less than 250 K. Normalized for a subset of features with a large rain volume (exceeding $10^4 \text{ mm h}^{-1} \text{ km}^2$) independent of the PF classification, features with TMI > PR in the Tropics tended to have a higher fraction of stratiform rainfall, higher IR cloud tops, more intense radar profiles and 85-GHz ice-scattering signatures, and larger rain areas, whereas the converse is generally true for features with PR > TMI. Subtropical-area PF bias characteristics tended not to have such a clear relationship (especially over the ocean), a result that is hypothesized to be due to the influence of more variable storm environments and the presence of frontal rain. Melting-layer effects in stratiform rain and a bias in the ice-scattering–rain relationship were linked to the TMI producing more rainfall than the PR. However, noting the distinct characteristic biases Tropics-wide by feature type, this study reveals that accounting for regime-dependent biases caused by the differing horizontal and vertical morphologies of precipitating systems may lead to a reduction in systematic relative biases in a microwave precipitation algorithm.

1. Introduction

Shortfalls in our observations and modeling of precipitation processes hamper our ability to model the current variability of the atmosphere and our ability to predict the impacts of climate change. Many techniques have been used to estimate the spatial and temporal

variability of global precipitation, including rain gauge networks, surface observations, and satellite methods using IR, passive microwave, and spaceborne radar sensors. However, sources of error in these estimates often stem from rainfall’s variability in both space and time or, in the case of the remote sensing of rainfall, physical indirectness of the inversion technique used to estimate rainfall. These difficulties are exacerbated in the Tropics and midlatitude warm seasons, for which rainfall often occurs in a mixed convective–stratiform mode. Passive microwave and spaceborne radar remote sensing rainfall algorithms are now relied on to correct less-direct infrared methods of estimating rainfall (e.g., Adler et al. 2000) and must accurately account for the characteristic passive microwave and radar microwave signatures of these modes of rainfall. Because climate–rainfall feed-

* Current affiliation: Radar Meteorology Group, Department of Atmospheric Science, Colorado State University, Fort Collins, Colorado.

Corresponding author address: Dr. Stephen W. Nesbitt, Department of Atmospheric Science, Colorado State University, Fort Collins, CO 80523-1371.
E-mail: snesbitt@radarmet.atmos.colostate.edu

backs are sensitive to regional rainfall variability, detailed validation of spaceborne precipitation estimates is necessary.

The Tropical Rainfall Measuring Mission (TRMM) satellite was launched in November of 1997 to study the variability of rainfall in the Tropics (Simpson et al. 1988) with a collocated suite of instruments designed to provide both radar reflectivity profiles and high-resolution passive microwave measurements. The platform allows quantitative, collocated comparisons of rain estimates from both types of sensors. Kummerow et al. (2001) report that estimates of rainfall Tropics-wide from the TRMM Microwave Imager (TMI) 2A12 version-5 algorithm exceed those from the precipitation radar (PR) 2A25 version-5 algorithm by 20% and 23% over land and ocean, respectively. These TMI-PR differences are due to many factors, including differing physics of the retrieval techniques (active vs passive microwave retrievals and their inherent assumptions) and some artifacts in the estimates. Going beyond identifying zonal rainfall biases among the estimates, this study seeks to diagnose the algorithms' rainfall differences by examining modes of rainfall on a regional and storm-type basis that are 1) responsible for a significant fraction of the rainfall in a given region, 2) classifiable by existing remote sensing techniques, 3) climatically important for their characteristic heating and divergence profiles, and 4) responsible for a unique but identifiable contribution to the differences in the rainfall estimates because of their characteristic hydrometeor profiles. In this vein, the classification of storms within the TRMM dataset is performed in hopes of using our added understanding of the modal properties of these systems to evaluate rainfall estimates in regions where they occur.

In examining the modes of rainfall from a horizontal-morphology perspective, the largest and most easily recognizable precipitation features (PFs) are mesoscale convective systems [MCSs (Zipser 1982), defined by remote sensing criteria by Houze (1993), Mohr and Zipser (1996), and Nesbitt et al. (2000)]. Although these features have been found to contribute more than 50% of the total rainfall in a given tropical rainy region (Rickenbach and Rutledge 1998; Nesbitt et al. 2000), significant rainfall occurs from systems not meeting MCS size or intensity criteria. In fact, many of the rainiest places in the world rarely see such organized systems. Rainfall modes from small, warm cumulus clouds through individual cumulonimbi to sub-MCS-sized cumulonimbus cloud clusters that do not meet MCS criteria contribute significantly to the rainfall in many areas. The microphysical and heating profiles of these systems likely differ considerably from those of MCSs; local and bulk contributions from these systems cannot be neglected if we are to understand the global climate (Short and Nakamura 2000). From a microwave remote sensing standpoint, however, these small-to-medium-sized systems may introduce rainfall estimate biases due to their size or their radiative signal being too small (beam filling)

or weak (lack of instrument sensitivity) to yield a signal in a given relatively large satellite footprint.

To quantify the biases in the rainfall estimates on a regional and storm-type framework, the method of this study will be 1) to examine the climatic-scale differences in the PR and TMI estimates, comparing them to other in situ and satellite estimates, and 2) to examine a shorter-term dataset of matched feature-by-feature estimates of PR and TMI rainfall in a global sense to identify regional and storm-type biases. On both climatic and system-by-system scales, ancillary observations from TRMM and meteorological understanding of regional and system-type modes of rainfall are used to decipher the differences in the precipitating systems that cause the algorithms to diverge from each other or other "ground truth" rainfall estimates.

2. Data and methods

This study evaluates two of the TRMM rainfall algorithms, the TMI 2A12 passive microwave algorithm (Kummerow et al. 1996, 1998, 2001), and the PR 2A25 radar algorithm (Iguchi and Meneghini 1994; Iguchi et al. 2000). Hereinafter, the 2A12 (2A25) algorithm rainfall estimates will be referred to as TMI (PR) estimates.

a. The TMI rain algorithm

The TMI is a nine-channel dual-polarized elliptically scanning passive microwave radiometer, which views the earth at a 52.8° incidence angle. It has a swath width of 759 and 873 km, corresponding to pre- and postboost conditions.¹ The sensor measures horizontally and vertically polarized brightness temperatures at 10.65, 19.35, 37.0, and 85.5 GHz, with measurements at vertical polarization measured at 21.3 GHz. Effective fields of view vary from 63 km × 37 km and 72 km × 43 km at 10-GHz to 7 km × 5 km and 8 km × 6 km at 85-GHz pre- and postboost conditions, respectively.

The TMI rain algorithm [historically known as the Goddard profiling algorithm (GPROF)] uses a Bayesian approach to match the observed brightness temperatures from a pixel with those from a database of simulated hydrometeor profiles from cloud-resolving-model simulations, coupled with a microwave radiative transfer model. Over ocean, the usefulness of both emission and scattering channels allows the efficient use of a Bayesian method to select hydrometeor profiles in the database from the full suite of brightness temperatures (Kummerow et al. 2001), where the physics of the algorithm relies on both emission-based (e.g., Wilheit et al. 1977, 1991; Prabhakara et al. 1992) and scattering-based (e.g., Spencer et al. 1989; Mugnai et al. 1990; Grody 1991;

¹ The TRMM satellite was boosted from a nominal altitude of 350 km to an altitude of 402.5 km during August of 2001 for fuel savings. This "boost" resulted in a decrease in the areal resolution of its sensors by roughly 30%.

Vivekanandan et al. 1991; Ferraro and Marks 1995) retrievals. In addition, a convective–stratiform separation algorithm is used over the ocean [see Olson et al. (2001) for details]. The emission-based technique, while being insensitive to the details of the drop size distribution (DSD), is highly sensitive to the assumed shape of the rain profile (which is supplied by the cloud model in GPROF), the assumed freezing-level height (Wilheit et al. 1977; Harris et al. 2000), and the beam-filling correction (Ha and North 1993) from its large-footprint size in the emission channels. Because of the TMI's larger footprint areas by a factor from 1.8 (85 GHz) to 200 (10 GHz) relative to the PR, it is expected that beam filling causes a more significant bias in the TMI estimates than in the PR estimates, especially in non-uniform rain. This uncertainty is likely exacerbated over ocean, where large-footprint low-frequency emission channels are used in combination with the high-frequency channels.

Over land, only scattering frequencies are useful for rain estimation, which yields too little information to use a Bayesian profile selection technique in GPROF (Kummerow et al. 2001) because of the high and variable microwave emissivity of land surfaces. Ice-scattering techniques have a major disadvantage in that they are inherently empirical because of the unknown phase, density, size distribution, shape, and orientation of the ice particles in the sample volume (Mugnai et al. 1990; Vivekanandan et al. 1991; Kummerow et al. 2001), as well as the empirical relationship used to relate the ice-scattering optical depth aloft and the rain rate underlying the ice layer. In version 5 of the TMI algorithm, it was decided to selectively match the GPROF cloud-model database with the ice-scattering–rain-rate algorithm created for operational use by the National Oceanic and Atmospheric Administration National Environmental Satellite, Data, and Information Service (NESDIS). The algorithm, outlined in Ferraro (1997), uses an empirically derived 85-GHz ice-scattering ground-based radar–rain relationship while also attempting to remove artifacts caused by snow cover and other low-emissivity surfaces (such as high soil moisture). It uses a scattering-index–rain-rate approach developed by Grody (1991). In addition, a global threshold of 22-GHz brightness temperature <262 K is used to attempt to mask low-emissivity snow, ice, and soil moisture areas (McCollum and Ferraro 2003). Pixels meeting this empirical threshold are set to zero rain rate in the algorithm and may introduce a negative bias in areas of actual precipitation over radiometrically cold surfaces (most often during subtropical cold seasons). However, this technique is sometimes unsuccessful in removing all cold surface artifacts (Ferraro et al. 1998), as will be seen in this study.

A source of uncertainty in the TMI algorithm is the representativeness of the simulated cloud profiles to clouds in nature. For example, the cloud model may have a tendency to place too little or too much ice in

its vertical profiles for a given rain rate, leading to a surface rain bias (Fiorino 2002). In addition, the use of as many varied simulations as possible, representing various radiative scenes, is desirable, but this desire is offset by the need for meaningful and computationally fast statistical convergence in the selection of a representative hydrometeor profile. The use of a limited number of profiles that likely differ from those occurring in nature is a major, hitherto unquantified, source of uncertainty in the TMI retrievals.

b. The PR rain algorithm

The PR is the first spaceborne rain radar. Because of engineering constraints, spaceborne radar capabilities are limited in power and wavelength selection in comparison with their ground radar counterparts—the former condition leads to a high minimum detectable signal of 16–18 dBZ for the PR preboost (Kozu et al. 2001), with a decrease in sensitivity of about 1.2 dB after the boost (returned power falls off with range r as $1/r^2$), and the latter condition leads to significant attenuation by precipitation at its transmitting frequency (wavelength) of 13.8 GHz (2.2 cm). However, the PR's great advantages are Tropics-wide coverage (within its 220-km preboost, 250-km postboost swath) in regions that are devoid of ground-based radar coverage, down-looking scan geometry that allows retrievals close to the surface (within 0.5–2 km), and excellent vertical resolution (0.25–1.5 km) when compared with ground-based scanning radar. The process of inverting the PR's measured reflectivity to attenuation-corrected equivalent reflectivity factor (Z_e) and rain rate is accomplished by the PR algorithm, which is detailed in Iguchi et al. (2000). Measured heights of the brightband and climatological surface temperature data are used to estimate the heights of liquid, mixed-phase, and frozen hydrometeors using the 2A23 convective–stratiform separation algorithm, which uses this information as well as horizontal reflectivity gradients (to try to correct for nonuniform beam filling) to constrain a globally assumed attenuation– and rain-rate–reflectivity (R – Z) relationship on a pixel-by-pixel basis. Factors that add uncertainty to the PR retrievals of rain rate include its global drop size distribution assumptions and Z – R inversion technique [see Atlas et al. (1999), Atlas and Ulbrich (2002), and Jameson and Kostinski (2002) for further discussion], and attenuation correction. Bias introduced into the PR rain estimates by these assumptions has yet to be quantified.

c. The PF database

Nesbitt et al. (2000) outline a method of creating a database of PFs in which PR and TMI data are matched onto the PR grid using a nearest-neighbor technique. In Nesbitt et al. (2000), contiguous areas within the matched PR–TMI dataset (including corner pixels) ≥ 4

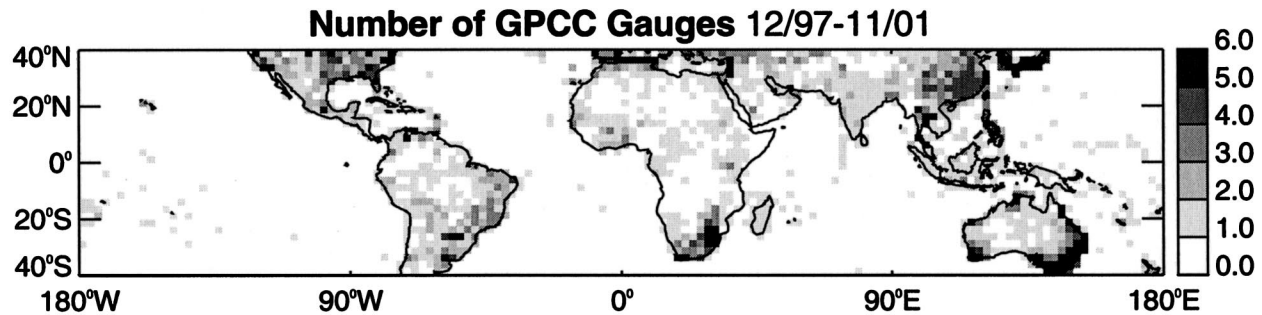


FIG. 1. Mean number of gauges in the 2.5° GPCC analysis for the period of Dec 1997–Nov 2001.

PR pixels in size of PR near-surface reflectivity ≥ 20 dBZ or TMI 85-GHz polarization-corrected temperature (PCT; Spencer et al. 1989) depressions ≤ 250 K are identified as PFs.

The current study differs slightly from the criteria of Nesbitt et al. in that PFs are defined to include any contiguous pixels within the PR swath having nearest-neighbor-matched TMI or PR rain rate > 0 mm h^{-1} (including corner pixels), with no minimum pixel count or 85-GHz PCT threshold applied. In Nesbitt et al. (2000), a four-pixel contiguous area threshold was used because the TRMM PR version-4 products contained significant low-reflectivity noise. In version 5 (the products used in this study), an improved filtering technique has been used that better removes instrument noise while retaining meteorological echo. Although some noise undoubtedly remains (mainly from sidelobes), the desire to examine the entire bias spectrum of precipitation features down to the smallest scales (i.e., individual cumulonimbus) outweighs the concern of including some low-reflectivity (and low rain volume) pixels in this study.

Most pixels with 85-GHz PCT < 250 K, in the absence of surface artifacts, should have a nonzero TMI rain rate, and so the inclusion of all raining pixels, for the most part, is inclusive of the Nesbitt et al. (2000) definition. This change in the precipitation feature definition results in the inclusion of 19% more raining pixels (those pixel features that are between the PR minimum detectable signal of 17 and 20 dBZ and have a size between 1 and 4 pixels); about 4% of the total PR near-surface rainfall is added. For each PF in this definition, the rain estimates for the PR and TMI are matched on a feature-by-feature basis, allowing a direct storm-type comparison between the PR and TMI estimates. If no rain is found in one of the two estimates, that feature is still included in the dataset. This study examines 1 yr of data from the postboost period of December 2001–November 2002. Despite the change in the criteria for selecting PF pixels, PFs are classified using the three categories as in Nesbitt et al. (2000):

1) PF without ice scattering (NI; no pixels containing PCT ≤ 250 K at 85 GHz), which are likely “warm rain” features that are too shallow or those features

that are too small to contain significant ice scattering at TMI resolution;

- 2) PF with ice scattering (WI; at least one pixel with 85 GHz PCT ≤ 250 K), which are features with significant optical depths of ice aloft but which are not large or intense enough to meet the MCS category; or
- 3) PF with an MCS (PF containing at least 2000 km² of contiguous area with 85-GHz PCT ≤ 250 K and 185 km² ≤ 225 K), which are defined to ensure a large convective system analogous to the Mohr and Zipser (1996) and Houze (1993) ice-scattering and radar MCS definitions, respectively.

Results using TMI data matched within PR swath only are denoted as TMI* in this study. In addition to several PR and TMI characteristics, minimum Visible and Infrared Scanner (VIRS) IR 10.7- μ m brightness temperature (T_b) and maximum 3-day-averaged TMI sea surface temperature (SST; Wentz et al. 2000) within each feature have been incorporated into the database. Three-day-averaged values are used instead of instantaneous values to mitigate missing-data problems in raining pixels (microwave SST retrievals are contaminated by emission from rain).

d. Gauge data

Monthly global rain gauge data are from the Global Precipitation Climatology Centre (GPCC) “Monitoring Product” (information was available online at <http://www.dwd.de/research/gpcc/e23.html>). The analysis is performed on a 2.5° \times 2.5° grid using an objective-analysis technique presented in Rudolf (1993). The data sources are quality-controlled globally exchanged synoptic weather reports (“SYNOP”) and monthly climate reports (“CLIMAT”) from roughly 6000–7000 stations. The GPCC gauge analysis is interpolated to points that contain no gauges (Rudolf et al. 1994), regardless of the number of gauges present; Fig. 1 shows the mean number of gauges per month in each 1° grid box in the Tropics for the period of December 1997–November 2001. Note that gauge coverage is concentrated in developed countries, which leaves a dearth of gauges in

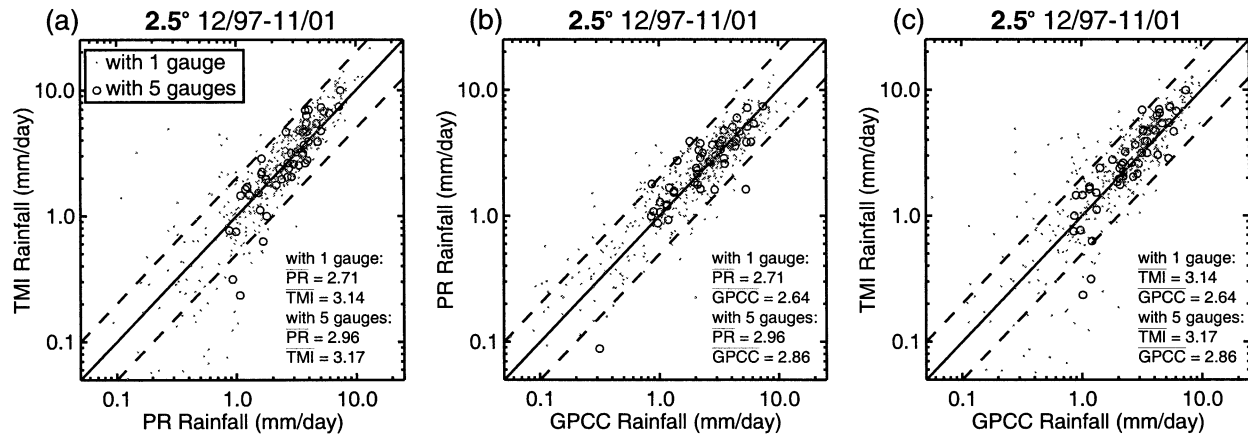


FIG. 2. Scatterplots of $2.5^\circ \times 2.5^\circ$ (a) TMI vs PR, (b) PR vs GPCC, and (c) TMI vs GPCC rainfall in grid boxes with at least one gauge (gray dots) and five gauges (open circles). Note the log–log axis; the solid line is the 1:1 line, and the dashed lines indicate a 100% difference. Mean rainfall values (mm day^{-1}) for each gauge number threshold are displayed.

many low-latitude areas. This sparsity presents a challenge in using such gauge analyses for satellite validation. In addition to the gauges' tendency to underestimate rainfall (e.g., in high winds), it has been found necessary that at least five gauges be in a $2.5^\circ \times 2.5^\circ$ grid box to reduce sampling errors to within 10% (Legates and Willmott 1990). This condition is met in only 8.4% of the over-land grid boxes in the GPCC dataset. Nicholson et al. (2003a) found that there was little bias in rain estimates when comparing GPCC grid boxes with less than five gauges with a high-resolution gauge dataset over West Africa, rather only the introduction of random error. In this study, GPCC boxes with >1 and >5 gauges are used, noting that tropical coverage is sparse, and rms errors of more than 25% may be introduced on the monthly time scale in boxes with only one gauge (Xie and Arkin 1995). In this study, 4-yr averages are presented, and so the random error component would be expected to lessen.

e. Comparing precipitation estimates of different sampling resolutions

Point measurements from gauges and the pixel sizes of the TMI and PR vary considerably in sampling resolution. Even when data are compared on a common grid resolution, representativeness error, which is defined by Tustison et al. (2001) as the error introduced by rescaling the data to a different resolution, may introduce important error in the comparison. This study does not make an attempt to address contributions to the total error by representativeness error in accounting for differences between the gridded estimates shown in section 3. In comparing the TMI and PR data in section 4, again note that the resolution of the TMI is at least a factor of 1.8 less than the PR (effectively a higher discrepancy over ocean because of the use of larger low-frequency footprints). Thus, instantaneous rain rates from the TMI would be expected to be lower than those

of the PR. This study does not attempt to match the two resolutions (mainly because the TMI resolution is effectively different over land and ocean because of the use of different channel combinations), and, as will be seen in this study, the fact that the TMI generally produces higher rain rates than the PR indicates that there are significant unresolved issues in one or both of the algorithms.

3. Global comparisons of long-term averages of rain estimates

Comparisons of the rain estimates on long temporal scales and large spatial scales can be used in a broad sense to help to mitigate the effects of random error to show algorithmic biases. Figure 2 compares the December 1997–November 2001 $2.5^\circ \times 2.5^\circ$ rain estimates on a log–log scale from the TMI, PR, and GPCC gauge analyses in grid boxes with at least one gauge (gray dots) and boxes with at least five gauges (black circles). Means of the two datasets appear in each panel. In Fig. 2a, the TMI estimates are found to be 16% higher than the PR Tropics-wide over land where one gauge exists, which is roughly consistent with the 20% figure quoted by Kummerow et al. (2001) given the different locations and time periods used. In areas with five gauges, the TMI is only 7% higher, but this result is likely due to the locations of sample points in the subtropics (see Fig. 1); the fractional bias is highest in the deep Tropics (Kummerow et al. 2001). The PR estimates more rainfall at lower rain rates, with the exception of a few outliers where the TMI is several factors greater than the PR. At higher rain rates, the TMI generally estimates more rainfall. In comparing the PR with the GPCC gauges in Fig. 2b, it is seen that the GPCC gauges are about 2% and 3% higher than the PR in locations with at least one and five gauges, respectively. The TMI estimates are about 16% and 9% higher than the GPCC estimates (Fig. 2c) for the two gauge number thresholds, respec-

tively. Here the scatter of the points is much higher for heavier rain rates than when comparing the GPCC and PR estimates, with most locations having TMI estimates higher than those of the GPCC above about 1 mm h^{-1} . Again, note the inclusion of more subtropical points in the dataset; Nicholson et al. (2003b) found that the TMI (PR) gives 32% (7%) higher rainfall than the GPCC estimates over the West African wet season in 1998, whereas the GPCC product was 4% lower than a gauge dataset containing hundreds of gauges in that region.

To show the geographic distribution of the estimates and their differences, Fig. 3 shows the rain estimates and their differences for the same 4-yr period shown in the scatterplots over both the land and ocean, where available. Figure 3 shows GPCC gauge rainfall, PR rainfall, and TMI rainfall (Figs. 3a–c, respectively), and absolute difference in rainfall between TMI and PR, PR and GPCC, and TMI and GPCC (Figs. 3d–f, respectively). The resolution of the plots is $2.5^\circ \times 2.5^\circ$. Rainfall values in Figs. 3a–c greater than 0.5 and less than 1.0 mm day^{-1} have been rounded to 1.0 mm day^{-1} , and values with locations with less than one gauge are not shown in Figs. 3e and 3f. Note in Fig. 3 that the rain estimates differ significantly as portrayed in the scatterplots in Fig. 2. The figure shows that the estimates agree in a qualitative sense, with the gauges (Fig. 3a) and PR (Fig. 3b) underestimating with respect to the TMI (Fig. 3c), especially in the deep Tropics. These disparities show up in the difference maps as well (Figs. 3d–f), where the TMI has more than 2 times the PR estimates over land areas like the Maritime Continent, equatorial Africa, tropical Australia, and the coastline areas in Chile, Baja California, western Africa, and the Middle East. The latter coastline problems are due to a screening problem in the TMI algorithm in which artifacts arise because of the coastline discontinuity in the algorithm (i.e., the transition between land and ocean algorithms). Over the ocean, large TMI positive differences show up over the Pacific ITCZ, and the percentage differences are higher in the central and eastern Pacific than in the western Pacific (not shown) because of lower rain rates in the east (Berg et al. 2002). Lesser positive TMI–PR differences (of $\leq 40\%$) exist over large areas of the Amazon basin, and the Atlantic and Indian Ocean ITCZ. On the contrary, the PR exceeds the TMI in several higher-latitude land regions, including inland areas in China, Mexico, and the United States, and South America, Africa, and Australia south of 30°S , as well as dry regions like North Africa, the Middle East, and ocean areas dominated by subtropical highs.

Comparisons of the PR and TMI rainfall with the GPCC gauge rainfall (where more than one GPCC gauge exists) appear in Figs. 3e and 3f, respectively. The PR overestimates exist with respect to the GPCC analysis over the Sierra Madre (however, it is likely that gauges are at lower elevations than the rainfall maximum), extending into the central United States (where gauge coverage is ample; McCollum et al. 2002). Other

areas with PR greater than GPCC occur in subtropical South America, mountainous areas like the Andes and Himalayas (where gauge coverage is poor along the slopes), western equatorial Africa, and the southern two-thirds of Australia. Over the Indian subcontinent, eastern Asia, the western African coast near the equator, and the Amazon, the PR tends to underestimate with respect to the gauges (all uniform rainfall areas). The same trend holds true over the Maritime Continent region (an area dominated by local effects), especially near the coastlines.

The TMI overestimates in most significantly rainy regions of the over-land Tropics with respect to the GPCC gauge analysis (Fig. 3f), with the notable exceptions of most of the over-land dry regions (apart from coastline and surface artifacts, e.g., the TMI's unreasonable overestimates in the Atacama Desert in Chile, south and east Asia, the southern two-thirds of Australia, and a few regions in the southeastern United States and Mexico).

The overestimate of the TMI with respect to the gauges over equatorial Africa is consistent with the findings of McCollum et al. (2000), who found that microwave ice-scattering rainfall overestimation is related to climatologically dry air and more aerosols and, thus, lower rainfall efficiency for a given amount of ice scattering (as compared with a more moist regime like the Amazon or the south Asian monsoon). Note, however, that the PR algorithm does not adjust its DSD parameters for low-level moisture conditions in a given region, which also introduces uncertainty in the PR retrieval. The finding that the TMI is greater than the PR in the Tropics agrees with the findings of Masunaga et al. (2002), who find that TMI vertically integrated precipitation water contents and rainfall are higher on a zonal basis than PR liquid water contents in the deep Tropics. A seasonal analysis was also carried out on the same 4-yr period (not shown), and it was found that subtropical warm seasons generally showed $\text{TMI} > \text{PR} > \text{gauge}$ biases (especially over land), whereas during the subtropical cold and transition seasons the TMI and, especially, the PR estimates were less than the GPCC gauge estimates over land [this $\text{TMI} < \text{PR}$ finding in cold seasons also agrees with Masunaga et al. (2002)]. The results of the analysis suggest that making conclusions on an annual or zonal basis may be misleading; regional cold and transition season and land-versus-ocean variations in the rainfall regime (and the TMI algorithm itself) are strong influences in the TMI–PR biases and TMI and PR biases with respect to the gauges.

Beyond these broad comparisons, however, it is difficult to use gauge comparisons for more than a long-term check of the TRMM algorithm performance and flagging of obvious artifacts because of the many caveats mentioned above and the inability to do instantaneous gauge–TRMM comparisons. There are few gauges in the GPCC analysis in the heaviest-rain areas as reported by the PR and TMI (locations with more

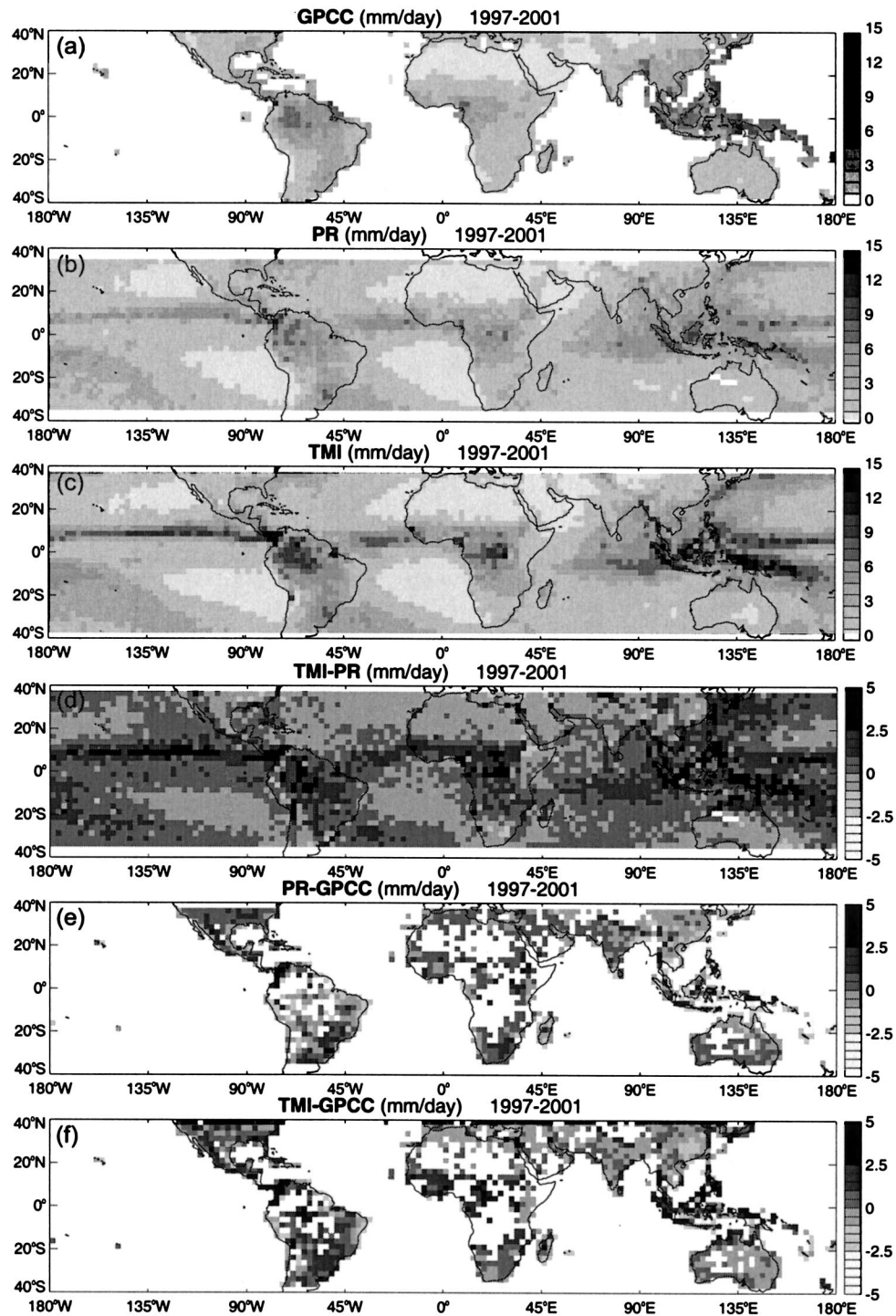


FIG. 3. Mean daily $2.5^\circ \times 2.5^\circ$ rain estimates and differences for all seasons for the period of Dec 1997–Nov 2001. (a) PR, (b) TMI, and (c) GPCC rainfall (mm day^{-1}), and differences (mm day^{-1}) between the (d) PR and TMI, (e) PR and GPCC, and (f) TMI and GPCC. White areas indicate (a)–(d) no data and (e)–(f) less than one gauge.

TABLE 1. The PR and TMI* unconditional rain rates (mm h^{-1}) and their percentage differences summed for all precipitation features types and by feature type.

		PR (mm h^{-1})	TMI* (mm h^{-1})	(TMI* - PR)/PR (%)
Total (sum of all feature types)	Land	2.51	3.13	24.7
	Ocean	2.36	2.98	26.3
MCS	Land	1.32	1.96	48.5
	Ocean	1.24	1.88	51.6
Features with ice scattering (WI)	Land	0.85	0.94	10.6
	Ocean	0.68	0.86	26.5
Features without ice scattering (NI)	Land	0.30	0.20	-33.3
	Ocean	0.47	0.28	-40.4

than five gauges never exceed about 9 mm day^{-1}). This fact, along with problems in comparing point and remotely sensed rain rates, other unknown sampling errors, and the inability to compare the estimates on a basis other than over long time scales, makes satellite-gauge comparisons of limited value for use in understanding the physical causes of differences in the TRMM rain estimates because we have limited additional information to lead us to algorithm deficiencies. A more detailed comparison of the PR and TMI algorithms' instantaneous estimates follows, hypothesizing that relative biases may be incurred in characteristic precipitation feature types.

4. Biases by feature type

The remainder of this study focuses on comparing the PR and TMI estimates, normalizing for sampling differences of the instruments. This normalization is accomplished by comparing the estimates within the PR swath only (TMI estimates within the PR swath are denoted as TMI*) for the period of December 2001–November 2002. Table 1 shows the unconditional rain rates for each precipitation feature type for both the PR and TMI* estimates over land or ocean. Unconditional rain rate is defined as the total rain volume within PFs (total or within the class noted) divided by the total number of raining (pixels within all PFs) and nonraining (pixels sampled outside PFs) pixels. For all features over land, the TMI* unconditional rain rate is 24.7% higher than that of the PR for this period (26.3% higher over ocean). The TMI* unconditional rain rate from MCSs is 49% and 52% higher than the PR MCS unconditional rain rate over land and ocean, respectively, which is a higher fraction than for the total rain-rate differences. Rain rates for WI are more in agreement; however, TMI* is still greater than the PR by 11% over land and 27% over ocean for these types of features. For NI features, the PR gives higher unconditional rain rates for both land and ocean categories by 17% and 54%, respectively. It is likely that beam filling and sensitivity errors in small NI features cause the PR to estimate higher unconditional rain rates here (the median area of such features is 25 km^2 , as compared with 700 km^2 for WI and 31 175 km^2 for MCSs).

To examine the spectrum of observed PR and TMI*

rain rates and biases as a function of rain rate, Fig. 4 is a contoured log-frequency diagram (with a histogram bin of $10^{0.05}$ times the axis value; a contour value of $-x$ means that a fraction of $1/10^{-x}$ of the distribution has that value) of TMI* versus PR $0.5^\circ \times 0.5^\circ$ gridded rain rates by precipitation feature type on a log-log axis. Note that the median of the histogram of PR rain rates as a function of TMI rain rate is also plotted (thick solid line), along with the 1:1 (thin solid) and 2:1 (thin dashed) bias lines. In this analysis, features' rainfall may be split among grids; however, their feature-type classification remains as if the storm were considered whole.

For MCSs over land (Fig. 4a), the median bias is toward the TMI* in grids with rain rates greater than about 0.3 mm h^{-1} ; the median bias steadily increases as rain rates increase to values greater than the roughly 50% value shown in Table 1. Over ocean (Fig. 4d), there is less scatter in the distribution; however, the median bias is always TMI* $>$ PR for the entire distribution, with a similar increasing TMI* bias trend toward higher MCS rain rates. A similar increasing bias with increased rain rate exists for WI (Figs. 4b,e). However, a trend for no bias over ocean (Fig. 4e) and a bias toward the PR for smaller WI rain rates (particularly below 0.6 mm h^{-1}) exists. This trend is again likely due to the effects of TMI sensitivity and beam filling at light rain rates and with small systems. These effects are particularly evident in the NI distributions over land and ocean (Figs. 4c and 4f, respectively) showing the strong trend toward higher rain estimates from the PR. This trend is more pronounced over ocean than over land, likely because of fewer artifacts in the data (note the outlying points with TMI* \gg PR) and the fact that there tends to be less of an ice-scattering signature over ocean (Nesbitt et al. 2000).

The estimates may also be examined on a storm-by-storm basis by examining biases in estimates of volumetric rain between the two instruments. Volumetric rain for each feature is calculated as the product of the sum of all its rain rates, its number of pixels, and the area of a pixel (resulting in units of $\text{mm h}^{-1} \text{ km}^2$). Figure 5 shows shaded, two-dimensional probability density functions (PDF) of individual PFs' total volumetric rain from the PR and TMI* on a log-log axis. Here the histogram bin size is $10^{0.05}$ times the axis value, and

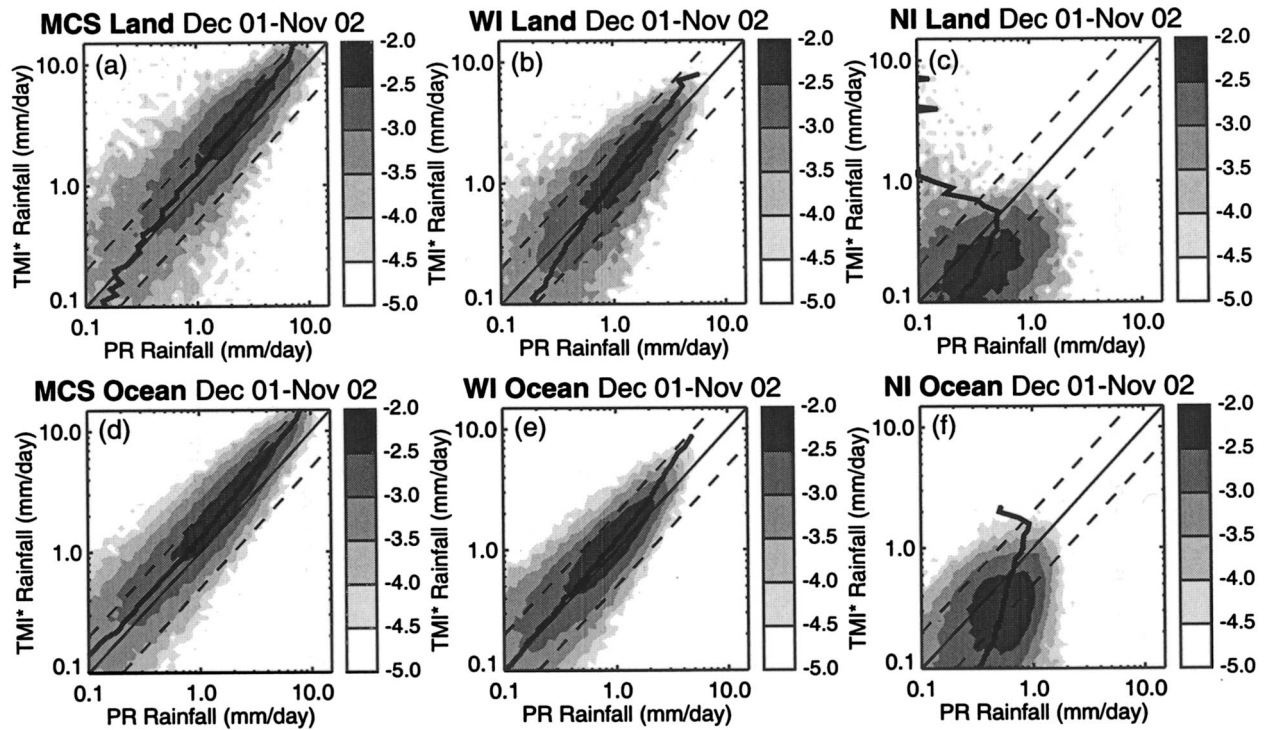


FIG. 4. Contoured log-frequency diagram of TMI* vs PR rainfall for the period of Dec 2001–Nov 2002: (a) MCSs over land, (b) WI over land, (c) NI over land, (d) MSC over ocean, (e) WI over ocean, and (f) NI over ocean. The median of the histogram is plotted (dark solid line); the solid and dashed thin lines are the 1:1 lines and 100% error lines, respectively.

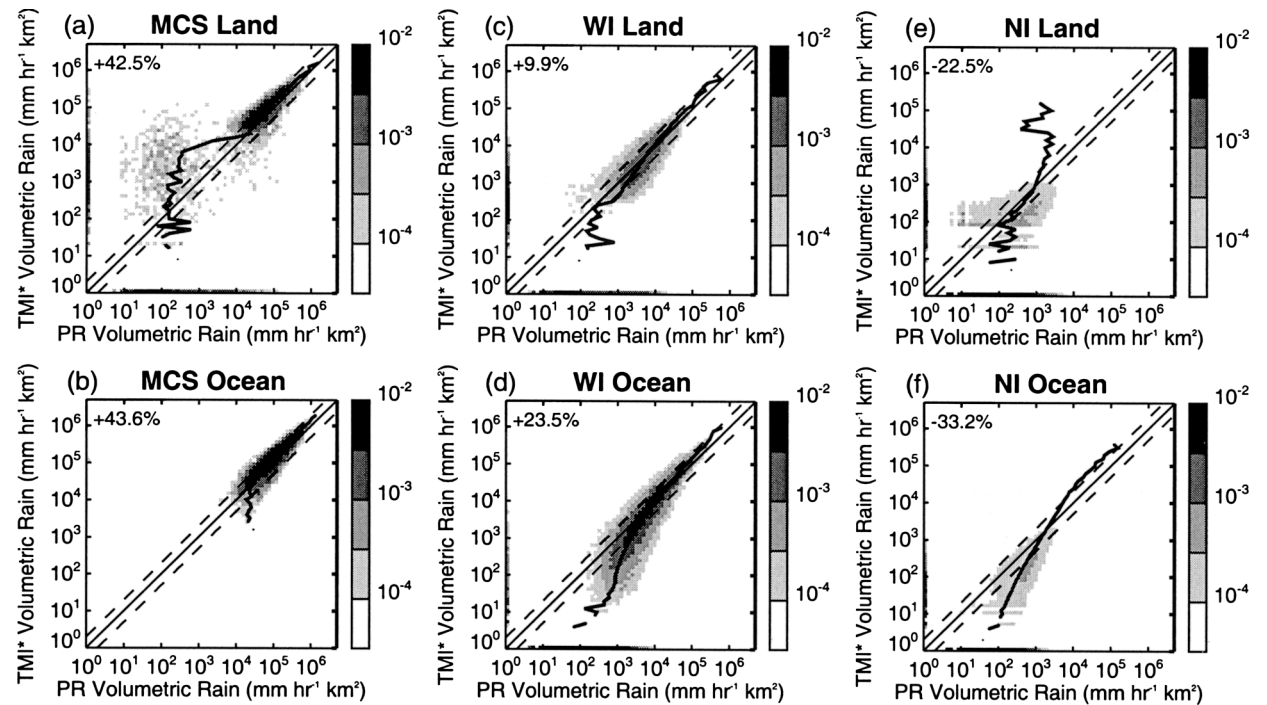


FIG. 5. Two-dimensional PDFs of TMI* vs PR feature-by-feature volumetric rainfall by PF type: (a) MCSs over land, (b) MCSs over ocean, (c) WI over land, (d) WI over ocean, (e) NI over land, and (f) NI over ocean. The median of the histogram is plotted (thick solid line); the solid and dashed thin lines are the 1:1 lines and 100% error lines, respectively. The number at upper left in each panel is the mean value of $(TMI - PR)/PR$ for each feature type.

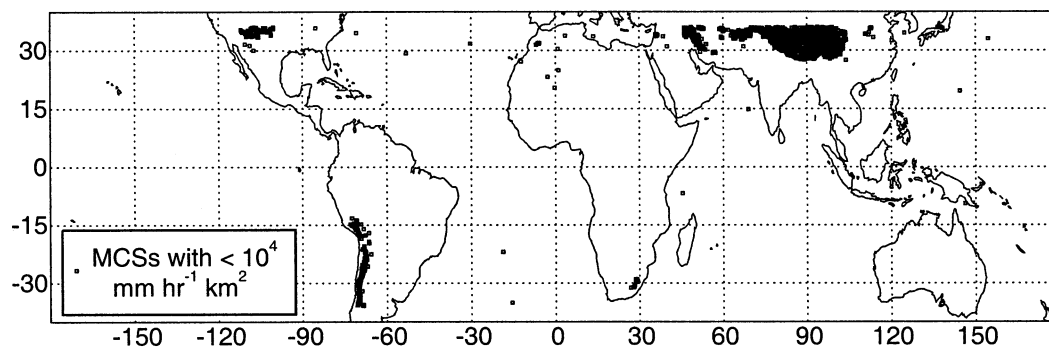


FIG. 6. Locations of MCSs with less than $10^4 \text{ mm h}^{-1} \text{ km}^2$.

one feature constitutes one point in the two-dimensional histogram. If a feature contains no rainfall by one of the instruments, its value is plotted along the x or y axis. Again, the median PR volumetric rain value is plotted as a function of TMI* volumetric rainfall with a dark solid line. The 2:1 and 1:1 lines are shown with thin-dashed and solid lines, respectively. The mean bias in system-by-system volumetric rain is shown in the upper-left corner of each panel. The mean volumetric rain bias values, when calculated feature by feature, agree within a few percent of the total rain-rate-by-feature-type values presented in Table 1. They differ slightly because the rain-rate values in the table are normalized by the latitudinal differences in sampling of the TRMM satellite.

When examining the biases by feature type, the MCS distributions over both land and ocean (Figs. 5a,b) above about $10^4 \text{ mm h}^{-1} \text{ km}^2$ consistently portray the pattern of the median volumetric rain bias, with the TMI* greater than the PR by roughly 45%. There is a spread of the distribution in this regime of more than a factor of 2 in both directions, however. As the distribution extends to lower volumetric rain values (toward, and below, $10^4 \text{ mm h}^{-1} \text{ km}^2$ over land in Fig. 5a), the scatter of points increases. Figure 6 shows the location of these features with $<10^4 \text{ mm h}^{-1} \text{ km}^2$ from both the PR and TMI* over land and ocean (they number 5476 out of the 20 576 total MCSs identified). Note their almost exclusive locations over mountainous terrain. The facts that rain rates in these PFs are well below the minimum detectable rain rate of the PR and are not typical of an MCS (a value of $3 \times 10^2 \text{ mm h}^{-1} \text{ km}^2$ over an MCS minimum area of 2000 km^2 is a mean rain rate of about 0.15 mm h^{-1}), that these features are rarely present over the ocean, and that the overwhelming majority of these features are located over subtropical mountainous areas indicate that these features below about $10^4 \text{ mm h}^{-1} \text{ km}^2$ are mostly artifacts caused by low-emissivity snow, ice, and radiometrically cold surfaces. They meet the MCS criteria in this study because of their considerable ice-scattering area and intensity at 85 GHz. TMI* rainfall is produced because the 21-GHz snow screen used in the NESDIS algorithm may not be properly triggered,

leaving remaining 85-GHz T_b depressions to produce TMI* rainfall. There may be some actual heavy precipitation detected by the PR within the TMI “MCS” ice-scattering area (which may be responsible for the points in the figure at which the PR retrieves more rainfall than the TMI), sidelobe noise, or ground clutter that the PR measures that is embedded within the TMI* scattering area that may explain PFs where the PR measures (or even in some cases exceeds the TMI*) rain in some storms.

With regard to Fig. 5, the mean biases of WI (Figs. 5c,d) over both land and ocean at volumetric rain values $>10^4 \text{ mm h}^{-1} \text{ km}^2$ are responsible for the TMI $>$ PR bias for this feature type (note that the log scale means that these heavily raining features weigh more in the mean). It appears that there is a higher population of WI near $10^5 \text{ mm h}^{-1} \text{ km}^2$ over ocean (which contain a characteristic bias in the TMI* direction), which leads to the greater TMI* positive bias in the mean over ocean for this feature type. Below $10^4 \text{ mm h}^{-1} \text{ km}^2$, the PR retrievals tend to contain more rainfall than the TMI*, eventually leading to a several-order-of-magnitude difference between the two sensors at the low end of the TMI* rain volume distribution. These differences are likely due to beam-filling issues (especially over ocean) and sensitivity issues (especially over land). The same pattern exists over land and ocean for NI (Figs. 5e,f); however, the sign of the PR–TMI difference is reversed relative to WI because of the different part of the rain volume spectrum populated between the two features (heavily raining features containing TMI* $>$ PR for WI vs lightly raining features containing PR $>$ TMI for NI). TMI* sensitivity issues with respect to shallow (including warm rain), narrow, or tilted (Hong et al. 2000) features would be expected to be more prevalent over land, where retrievals rely solely on ice-scattering signature.

5. Physical insights into the PR–TMI biases

To examine the bias characteristics of features for which biases are due more to algorithm physics rather than sensitivity and beam-filling issues in small features,

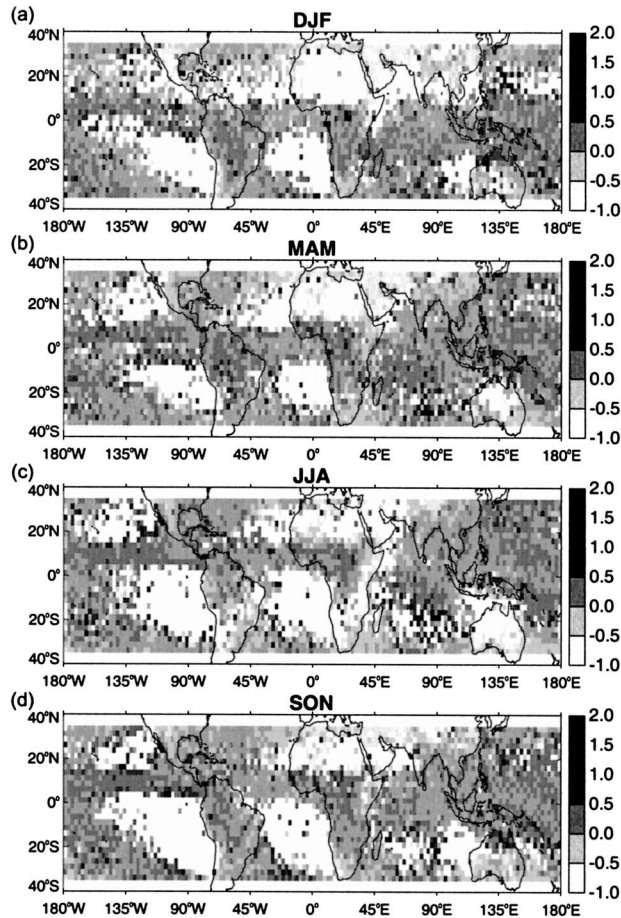


FIG. 7. Mean system-by-system $(TMI^* - PR)/PR$ for LRV features by 3-month season: (a) DJF 2001/02, (b) MAM 2002, (c) JJA 2002, and (d) SON 2002.

PFs with $>10^4 \text{ mm h}^{-1} \text{ km}^2$ (according to both the PR and TMI^* estimates) have been placed into a subset and will be examined for their characteristics for the remainder of the study. Note that these features (which number 50 890 out of 6.52 million PFs in the 1-yr dataset) are responsible for 76% of the total PR rainfall. This subset of features with large rain volume will be referred to as LRV features.

The seasonal mean bias as measured by $(TMI^* - PR)/PR$ for LRV features, gridded to $2.5^\circ \times 2.5^\circ$, is shaded in Fig. 7. In December–January–February (DJF; Fig. 7a), note that many areas in low latitudes contain biases toward the TMI^* exceeding 50%, including many areas where rainfall is heavy such as the oceanic ITCZ, most of lowland South America, and the Congo. The TMI^* rainfall is greater than that of the PR in most subtropical areas of the Southern Hemisphere as well, although there are some small areas near the Andes, South Africa, and Australia where the PR is higher. Over the Northern Hemisphere in many areas (especially over land), however, the PR is higher than the TMI^* .

As the season changes to March–April–May (MAM;

Fig. 7b), there are still many areas in the Northern Hemisphere that contain a bias toward the PR. However, TMI^* positive biases appear along the Gulf Coast and south Asia. The Tropics remain, for the most part, biased toward the TMI^* ; however, many Southern Hemisphere areas now have an increasing trend toward equal rain estimates (i.e., southern South America) or $PR > TMI^*$ (near South Africa and Australia). During the northern summer [June–July–August (JJA; Fig. 7c)], most lowland areas now have a tendency toward $TMI^* > PR$; however, mountainous areas such as the Sierra Madre and the Tibetan Plateau still have $PR > TMI^*$. Many Southern Hemisphere subtropical areas have no difference in JJA (including most of the Southern Ocean storm track) or are biased toward the PR (many land areas, including subtropical South America). In September–October–November (SON; Fig. 7d), many areas in the subtropical Southern Hemisphere return to biases toward the TMI^* ; the opposite trend is seen in the subtropical Northern Hemisphere, where previous warm-season biases change to more-agreeing rain estimates or $PR > TMI^*$. In general, these seasonal trends in which subtropical cold-season areas tend to have $PR > TMI^*$ while tropical and subtropical warm-season areas have $TMI^* > PR$ are in agreement with the findings of Masunaga et al. (2002). What is causing this reversal of bias characteristics as a function of region and season?

To investigate the remotely sensed properties of LRV features that may yield insights into the characteristic physical differences that cause differences between the PR and TMI^* , Figs. 8 and 9 present the cumulative distribution function (CDF) of several physical attributes related to the horizontal and vertical structure of the sample of LRV features. In the figures, the set of LRV features has been divided two ways to examine the regional characteristics of features with biases in both directions. Noting that tropical and subtropical features have different bias characteristics, Fig. 8 shows LRV features only within 20° latitude of the equator, while Fig. 9 shows features at $\pm 20^\circ$ of the equator. To examine differential physical characteristics between features with biases in both directions [ranked according to their $(TMI^* - PR)/PR$ values], those in the bottom 25th percentile (with the highest fractional bias toward the PR) and those in the top 25th percentile (those with the highest fractional bias toward the TMI^*) are grouped and labeled as $PR > TMI^*$ and $TMI^* > PR$ in the figures. The statistical distribution of each characteristic is compared between the two groups of features. To examine vertical profile information of the two groups of features, ice-scattering microwave PCTs, VIRS IR brightness temperatures, and radar profiles are examined. Structural differences in the horizontal direction are examined by comparing rain and ice-scattering area and convective–stratiform characteristics.

CDFs of VIRS minimum $10.7\text{-}\mu\text{m}$ brightness temperatures and TMI minimum 85-GHz PCTs are compared over land and ocean for the Tropics in Figs. 8a

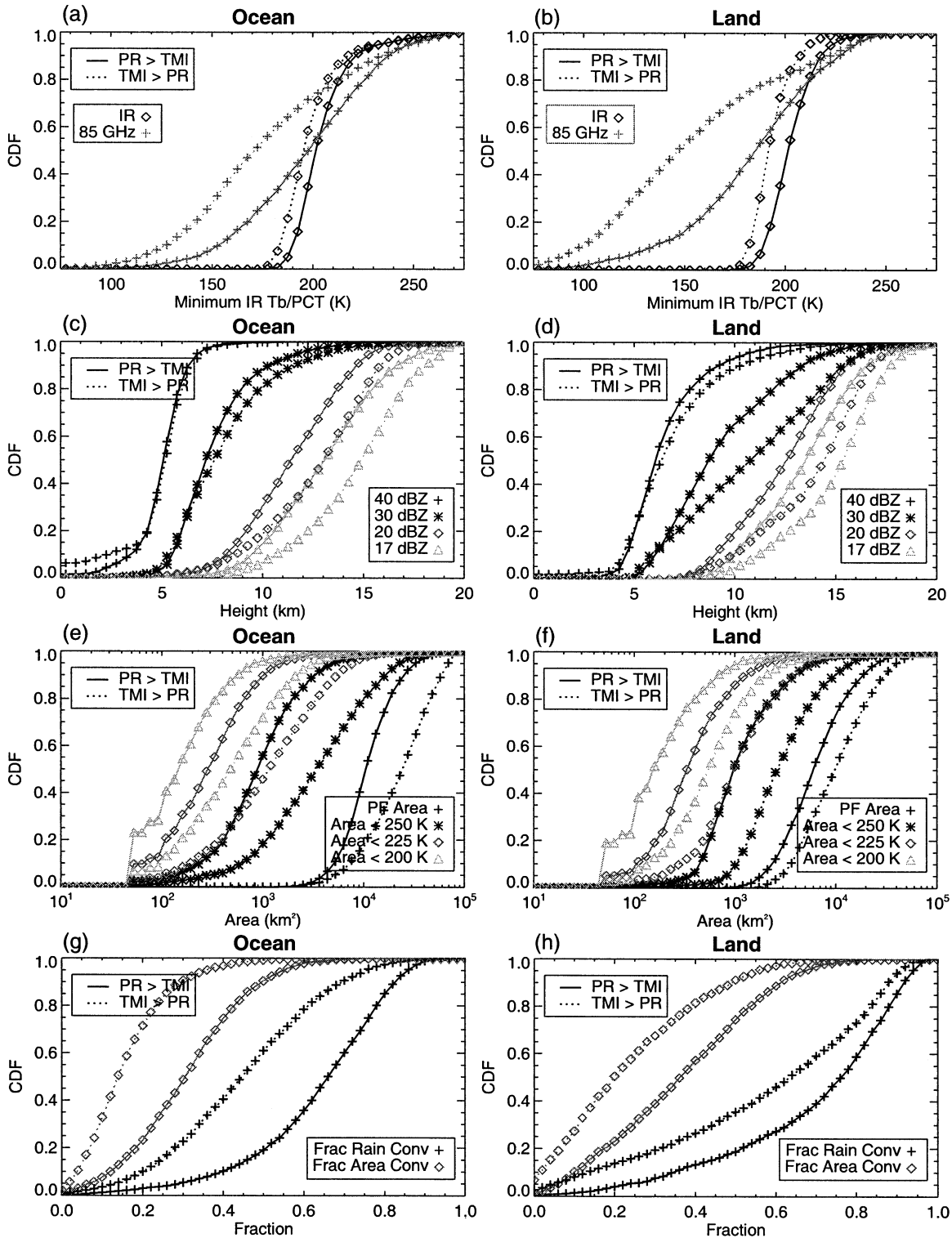


FIG. 8. CDFs of PF characteristics of those features within 20° latitude of the equator in the top 25th percentile of features with lowest (solid line) and highest (dashed line) $(TMI^* - PR)/PR$ over (left) ocean and (right) land. The symbol type indicates the parameter plotted: (a) minimum 85-GHz PCT (K); (b) minimum VIRS 10.7- μm T_b ; (c) maximum 40-, 30-, 20-, and 17-dBZ echo-top height (km); (d) and (e) PF area and 85-GHz PCT areas less than 250, 225, and 200 K (km^2); (f) and (g) fraction of PF area and rain that is convective.

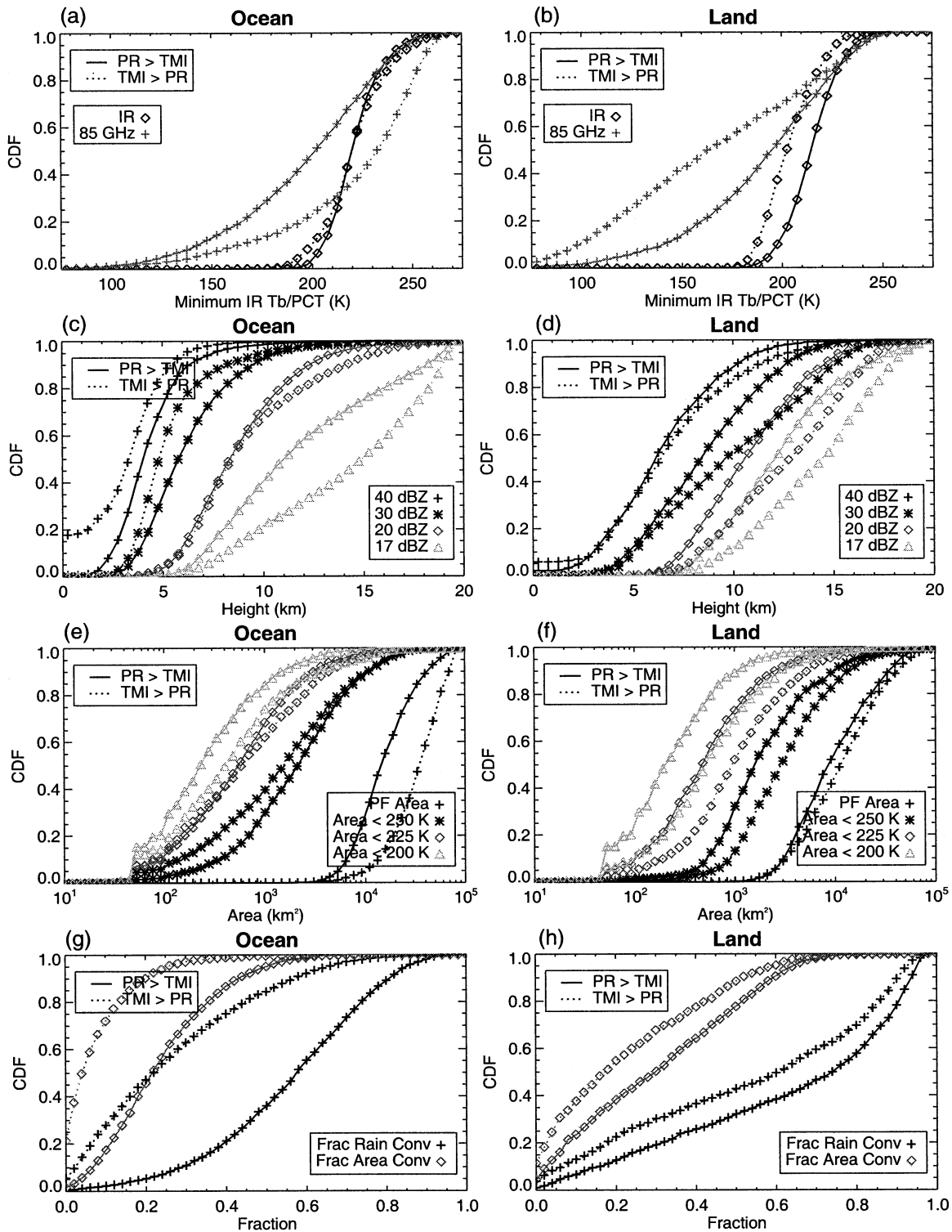


FIG. 9. Same as Fig. 8 but for features at $\geq \pm 20^\circ$ latitude.

and 8b. Over both ocean (Fig. 8a) and (Fig. 8b) land, LRV features with TMI* > PR have characteristically greater optical depths of ice and higher IR cloud tops than features with PR > TMI*. The differences are more

extreme over land (a median difference of 30 K at 85 GHz), caused either by a greater dynamic range in the parameter space or by the lack of constraint of all nine TMI channels in the retrievals over land. The distri-

butions of PR-derived maximum echo-top-height distributions at the 17- (near the PR's minimum detectable signal), 20-, 30-, and 40-dBZ levels over ocean (Fig. 8c) and land (Fig. 8d) reveal that 17- and 20-dBZ echo-top heights tend to be 1–2 km higher in features with $TMI^* > PR$ over both land and ocean. Over land, 30-dBZ echo-top heights are also several kilometers higher in $TMI^* > PR$ features while over ocean they are less than 1 km higher at most. Distributions at 40 dBZ are not sensitive to the bias over ocean, whereas there is a slight tendency for features with $TMI^* > PR$ to have higher 40-dBZ heights over land.

The distribution of total raining area and area of 85-GHz PCT less than 250, 225, and 200 K (as proxies for convective area) over the Tropics for the two bias groups is investigated in Figs. 8e and 8f over land and ocean, respectively. The difference in total area distributions is greater over ocean, but both land and ocean features with $TMI^* > PR$ have larger total areas than features with $PR > TMI^*$. However, ice-scattering areas within the rain area (for all three PCT thresholds) are larger for $TMI^* > PR$ features over both land and ocean. Figures 8g and 8h examine the distribution of the fraction of LRV feature area and rainfall that is classified as convective “certain” or “probably” according to the PR classification scheme and rainfall estimates. Over land, and particularly over ocean, the subset of features with $TMI^* > PR$ contains lower fractional coverage and rainfall classified as convective by the PR. This suggests that features with a lower (higher) convective (stratiform) area and fractional rainfall contribution tend to have $TMI^* > PR$.

Over the subtropics, the distributions of 85-GHz PCT (Fig. 9a) for the two bias groups switch position, with features with $PR > TMI^*$ now having more intense ice-scattering signatures. This is not the case over land; however, the distributions become much more similar when only the cold seasons are examined (not shown). In addition, the distributions of 30- and 40-dBZ echo-top heights over ocean for the two bias groups (Fig. 9c) exchange order; now, features with $TMI^* > PR$ have lower 30- and 40-dBZ heights. Note the larger areas (panels e) and higher fractions of stratiform rain (panels g) over the ocean for LRV features with $TMI^* > PR$ in the subtropics (Fig. 9) as opposed to the Tropics (Fig. 8). This points to different modes of precipitation physics over the subtropical oceans as compared with the Tropics, suggesting with such large stratiform fractions and weak ice-scattering signatures and radar profiles that these LRV features with $TMI^* > PR$ in the subtropics are likely large frontal systems that are mostly stratiform rain. Stratiform rain rates are commonly overestimated by the TMI^* algorithm, because the radiative effects of the melting layer are not included in the cloud-resolving model database in the version-5 TMI algorithm. The melting-layer hydrometeors in stratiform precipitation increase emission at all TMI frequencies (Olson et al. 2001), which leads to a positive bias in instantaneous

rain-rate estimates of up to 100% (Bauer et al. 1999). This melting-layer issue is likely a major cause of the positive TMI^* bias over ocean, where emission channels are used in the retrievals. In addition, this bias likely has more of an effect in areas with higher stratiform rain fraction (thus, errors in melting-layer physics are more important). As an example, note that the maximum in $TMI^* > PR$ fractional bias near 135°W in the ITCZ in Fig. 7 is collocated with the maximum of PR stratiform rain fraction shown by Schumacher and Houze (2003, their Fig. 3). This implies that proper identification of stratiform rain areas, coupled with a correction in melting-layer physics in the TMI algorithm, will serve to reduce this positive bias over both subtropical and tropical ocean areas. This overestimate is not seen to such an extent over subtropical land areas because the features are more dominated by convective rainfall (Fig. 9h) and tend to behave more like those in the Tropics.

Figures 10–13 examine the distribution of LRV feature properties as a function of the PR– TMI^* rainfall bias over ocean (Fig. 10) and land (Fig. 11) areas within 20° of the equator and over ocean (Fig. 12) and land (Fig. 13) areas at $> \pm 20^\circ$ latitude. In each of these four figures, the panels display a shaded log-frequency histogram of TMI minimum 85-GHz PCT (panels a), PR fraction of rain stratiform (panels b), PR maximum 20-dBZ (panels c), and 30-dBZ (panels d) echo-top height, VIRS minimum 10.7- μm T_b (panels e), and Wentz et al. (2000) 3-day-averaged TMI SST (panels f) (over ocean only) for each LRV as a function of each feature's value of $(TMI^* - PR)/PR$. The median and standard deviation of the bias values as a function of the parameter plotted on the y axis is plotted with the solid and thin lines and error bars, respectively. In addition, the straight line displays a regression fit to only the data observed at the -2.4 level to remove outliers and examine bias trends in the features' parameter space observed more frequently.

Over the tropical oceans, there is a trend for features with more intense 85-GHz peak ice scattering signatures (Fig. 10a) to become more biased toward the TMI^* . Stratiform rain fraction contains a strong trend with higher stratiform rain fractions leading to TMI^* values that are higher than those of the PR, another clue toward melting-layer overestimation in the TMI algorithm. The distribution of 20-dBZ maximum echo-top heights (Fig. 10c) also shows that increasing peak convective intensity leads to increased bias toward the TMI^* ; the distribution of 30-dBZ echo-top heights shows a much smaller signal. Minimum IR T_b distributions show that features with colder cloud tops tend to increase the TMI^* bias. It appears that there is little relation between the PR– TMI^* bias in these LRV features and SST over the tropical oceans (Fig. 10d).

The tropical land area 85-GHz PCT–bias relationship (Fig. 11a) is similar to that of areas over ocean, given the more intense distribution of 85-GHz PCTs over land.

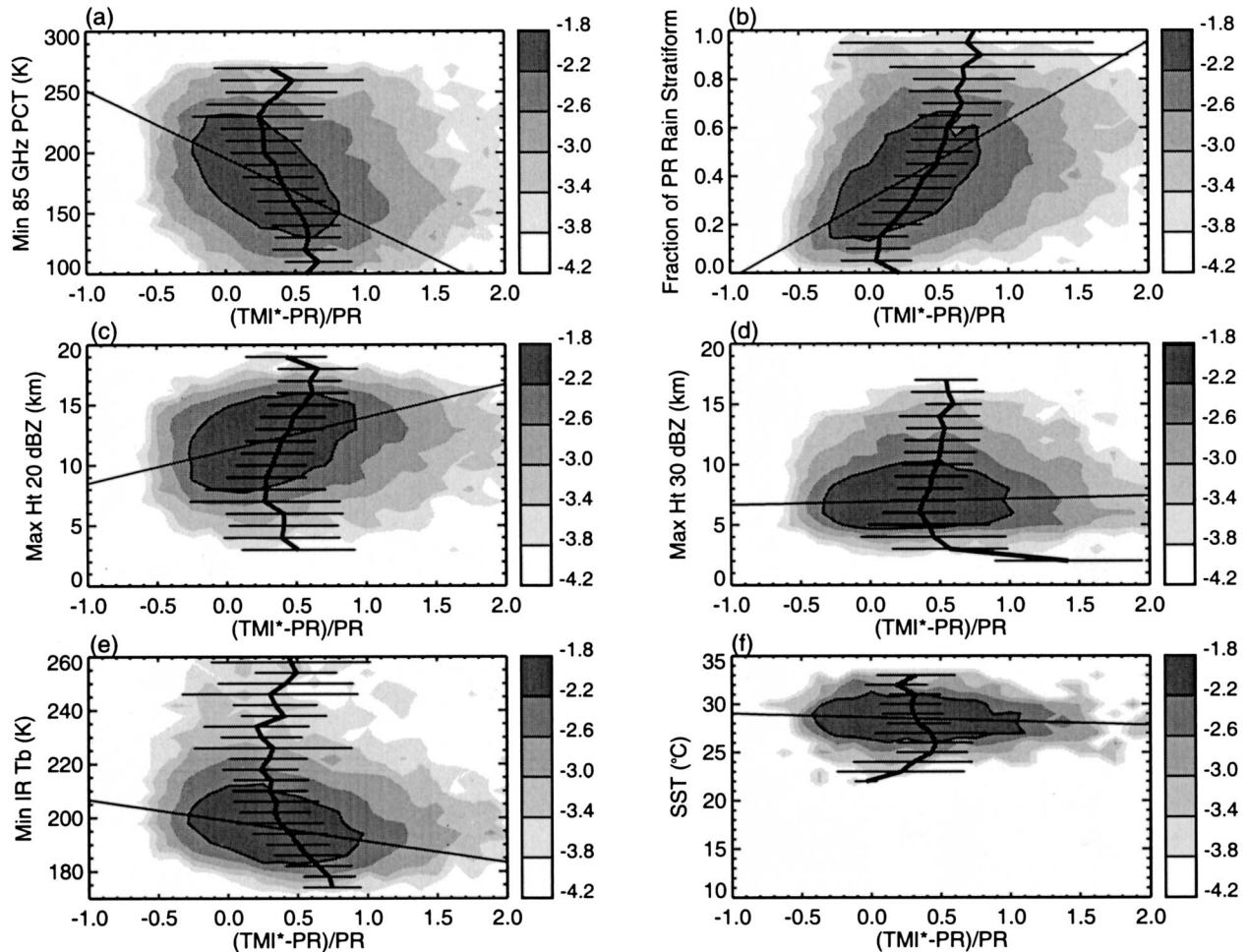


FIG. 10. Contoured log-frequency diagram (shaded) of selected PF characteristics vs $(TMI^* - PR)/PR$ over ocean within 20° latitude of the equator. The median (dark line) and standard deviation (thin error bars) of $(TMI^* - PR)/PR$ for each histogram bin along the vertical axis are plotted.

Over land, TMI emission channels are not used in the algorithm, and so the stratiform fraction would not be expected to influence land retrievals as over ocean. In (Fig. 11b), the TMI^* -PR relationship is expectedly weaker over land than over ocean (Fig. 10b); it appears that there is a general overestimation by the TMI^* relative to the PR on the median. Maximum echo-top heights at 20- (Fig. 11c) and 30-dBZ (Fig. 11d) show that higher heights tend to increase the bias toward the TMI^* . The 30-dBZ relationship was not as significant over the ocean (Fig. 10d). Minimum IR T_b over land (Fig. 11e) shows a tendency for decreasing minimum cloud-top temperature with increasing TMI^* bias. Note that the regression lines for 85-GHz PCT (panels a), maximum height of the 20-dBZ echo (panels c), and minimum IR temperature (panels e) are remarkably similar over ocean (Fig. 10) and land (Fig. 11).

In examining the subtropics in contrast with the Tropics, it is important to note the variability in the thermodynamic structure of the atmosphere (affecting the

freezing level and tropopause height, thereby influencing the vertical structure of precipitating systems and, thus, the radiative transfer) and to note the differing modes of rainfall occurring in the LRV-features subset (composed of a number of midlatitude frontal systems as opposed to tropical convective systems); these factors affect the performance of the algorithms and change their bias characteristics. Figure 12 examines the bias-attribute relationships over ocean at $>20^\circ$ latitude. The minimum 85-GHz PCT relationship is reversed from that over the Tropics, with LRV features with higher PCTs having a more positive TMI^* bias. The predominance of over-ocean subtropical LRV features with $TMI^* > PR$ is also shown throughout the year in Fig. 12, especially in the western Pacific storm track. Again, it appears that increasing the stratiform rain fraction over ocean in the midlatitudes causes increased TMI^* rain rates relative to the PR (Fig. 12b), probably due to melting-layer emission. The relationship between 20-dBZ heights and the TMI^* -PR bias (Fig. 12c) over the

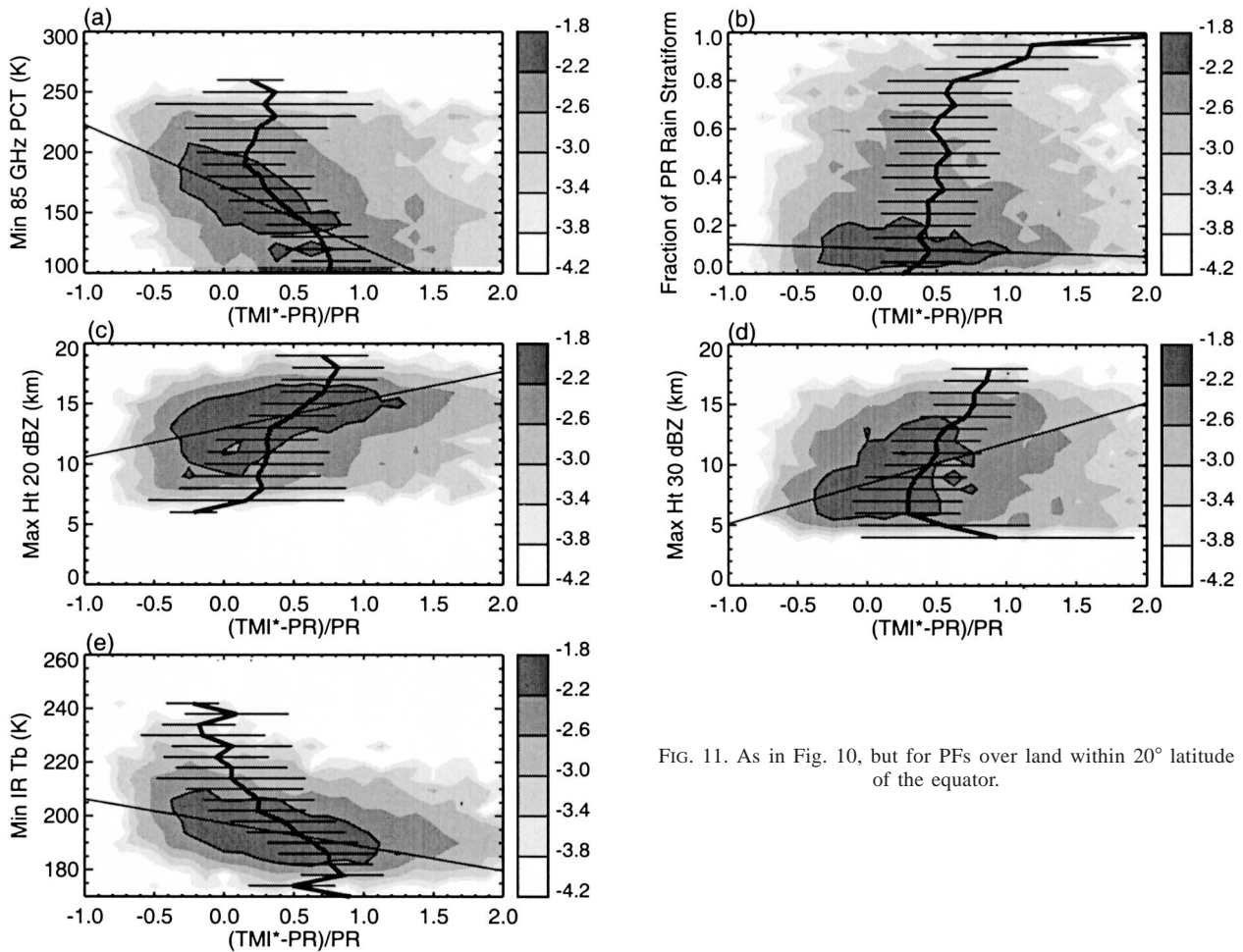


FIG. 11. As in Fig. 10, but for PFs over land within 20° latitude of the equator.

subtropics appears to have little bias information, although it appears that there may be two branches to the trend—one similar to the Tropics, extending along the median line for deeper convective features, and one following a trend similar to the regression line that may be due to midlatitude systems. There is little information in the over-ocean maximum height of the 30-dBZ relationship (Fig. 12d). Lower minimum IR brightness temperatures have a slight tendency to be associated with an increased TMI* bias, although it appears that there may again be two branches to the distribution roughly following the median and the regression lines, respectively. The regression line indicates a relationship between warmer SSTs in the subtropics and increased TMI* bias, although there is significant scatter and the median line only shows a variation of about 20%.

Over subtropical land areas, the TMI algorithm only uses 85-GHz ice-scattering information for its retrievals, and so freezing-level height is not an input to the algorithm. Freezing-level variations in nature only serve to define the lower boundary of the ice-scattering layer. Over these areas (Fig. 13), the relationship between lower minimum 85-GHz PCTs and a rainfall bias toward

the TMI* (Fig. 13a) is again present, as over the tropical land areas. Over the Tropics, the fraction of rain stratiform does not appear to influence the TMI*-PR differences; roughly a 20% bias extends throughout the distribution. Radar echo-top height-bias trends over subtropical land areas (Figs. 13c,d) are similar to those over tropical land areas (Figs. 11c,d). For minimum IR brightness temperature (Fig. 13e) the trend is similar; however, the parameter space of IR T_b is shifted to warmer temperatures, likely because of lower tropopause heights.

6. Summary and discussion

This study shows that the TRMM PR and TMI rainfall estimates agree within 25% Tropics-wide when normalized for sampling within the PR swath (cf. Kummerow et al. 2001; Masunaga et al. 2002). The TMI was shown to be, on average, 16% (7%) higher than the GPCC gauges, with the PR greater than the gauges by 3% in locations with one and five GPCC gauges in a 2.5° × 2.5° box. However, it is emphasized that significant regional and seasonal biases exist among the

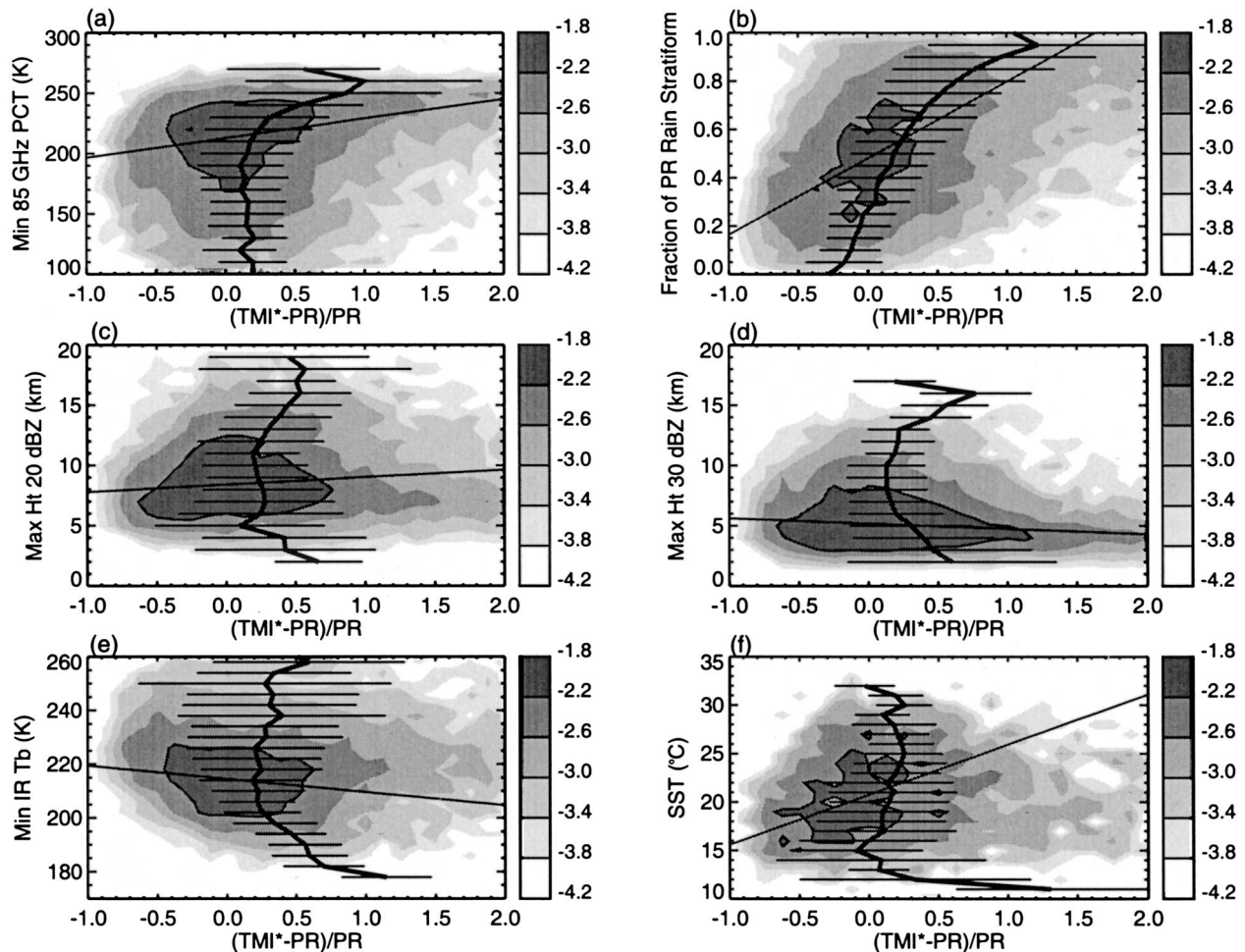


FIG. 12. As in Fig. 10, but for PFs over ocean at $> \pm 20^\circ$ latitude.

version-5 TRMM PR and TMI products and GPCC gauge products, often exceeding 100% on a regional basis. The paucity of GPCC gauge stations in the deep Tropics in particular must be taken into account in understanding quantitative remote sensing–GPCC gauge comparisons in many gauge-sparse regions (e.g., central Africa), because it introduces significant bias and random sampling error in the gauge network estimates. Results of regional high-resolution over-land gauge measurements and TRMM by Nicholson et al. (2003b) over West Africa and over Brazil by Mota (2003) agree with the TMI generally overestimating relative to the PR, with the PR being closer to the “truth.” Over ocean, Serra and McPhaden (2003) have shown that the PR may be underestimating relative to the TMI, with the TMI close to gauges for buoy gauge locations over the tropical Pacific. Given the regional variability in cloud system types (Nesbitt et al. 2000; Petersen and Rutledge 2001; Schumacher and Houze 2003) and the different algorithms used in the TMI method over land and ocean surfaces, these results are not surprising. However, further and smarter ground truth in terms of making val-

idation measurements in the proper meteorological context is needed to decide whether the TMI or the PR is more accurate, which remains an open question. Determining the portability of ground validation measurements from one location to another remains a significant challenge in satellite rainfall validation.

Table 2 summarizes the primary findings of the TMI–PR comparisons performed in this study. In comparing 4 yr of estimates Tropics-wide, and for 1 yr of direct storm-by-storm comparisons, the TMI estimates are generally higher than those from the PR in the deep Tropics and during the warm seasons in midlatitude locations. This result is in agreement with the result of Masunaga et al. (2002), who find that TMI near-surface precipitation water content values at low latitudes are higher than those of the PR; however, their study links this difference to a bias in the PR’s attenuation correction, causing low rain rates. This study links the TMI overestimates over ocean relative to the PR in LRV features (systems with $> 10^4 \text{ mm h}^{-1} \text{ km}^2$) with features with high stratiform rain fractions. A positive bias in the TMI algorithm has been attributed to emission from

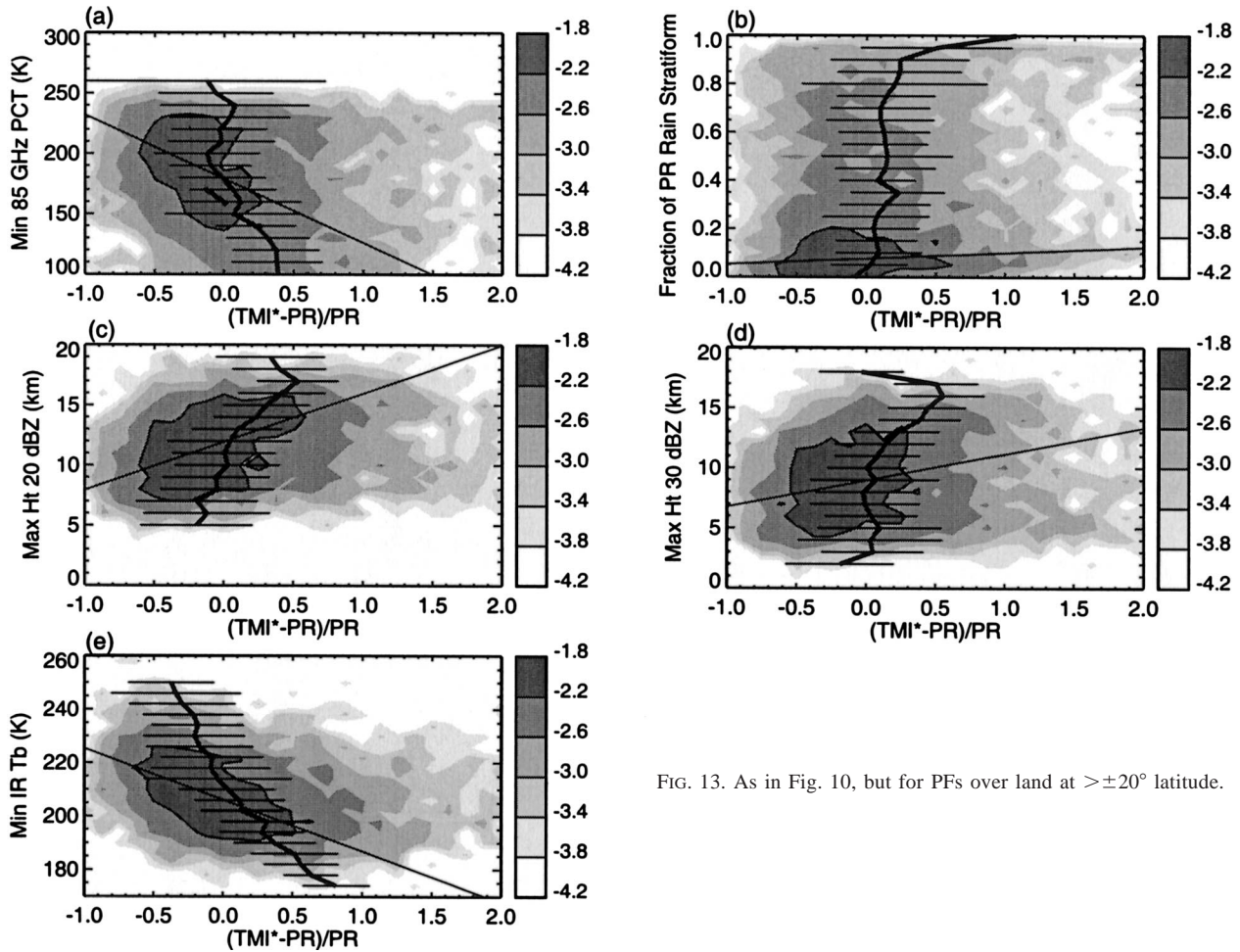


FIG. 13. As in Fig. 10, but for PFs over land at $\geq 20^\circ$ latitude.

TABLE 2. Factors identified in this study that affect TMI*-PR rain-rate differences.

Parameters that affect the algorithms relative to each other	Discussion
Melting-layer emission	Ocean: Noninclusion of melting-layer emission leads to increased TMI rain rates relative to PR with increasing stratiform fraction. Land: Emission channels not used, small effect in ice scattering retrievals at 85 GHz.
Convective intensity parameters according to min 85-GHz PCT, min VIRS IR T_b , and max PR echo-top heights (<30 dBZ)	Ocean: TMI increases relative to the PR as intensity increases, could indicate unrepresentativeness of cloud model database, or intensity related to stratiform fraction or nonuniform beam filling. Land: Direct relationship between intensity and increase in TMI rain rates relative to the PR, due to uncertainty in ice scattering-rain rate relationship; nonuniform beam filling less of a factor than over ocean because of smaller footprints.
TMI sensitivity, beam filling	Ocean: Uncertainty in nonuniform beam-filling correction, small convective features will be smeared out or missed. Land: Ice-scattering signature not produced for shallow rain, small convective features will be smeared out or missed.
Seasonal, regional variations in SST, atmospheric profiles	Ocean: Improper freezing-level-height assumption where SST, synoptic situation varies, highly stratiform frontal systems. Land: Changes in storm height, low-level moisture, and vertical shear may vary ice scattering-rain relationships
Radiometrically cold surfaces	Land: Unknown and changing emissivity of land surface makes screening of artifacts difficult.

the melting layer that is not accounted for in the current version 5 of the TMI algorithm (Olson et al. 2001; Kummerow et al. 2001). The increase in emission primarily by water-coated aggregates above the freezing level has been shown to increase passive microwave rain-rate retrievals by up to 100% (Bauer et al. 1999), especially in hydrometeor profiles with less ice optical depth above the emission layer. This effect would cause a positive TMI bias over ocean both in the Tropics and subtropics. This bias was found to be a function of rainfall system size and stratiform fraction. Melting-layer-caused biases were preferentially evident in large features (MCSs, presumed frontal systems in the subtropics) that contain a higher fraction of stratiform rain than in smaller, more isolated features (WI, NI). Convective intensity and cloud-top height was also positively correlated with TMI overestimates relative to the PR (particularly at low latitudes). This result may be due to the inappropriate selection of hydrometeor profiles by the TMI algorithm's Bayesian scheme or to differences between the selected cloud model profiles and nature. However, it is hard to say because storm intensity and areal coverage characteristics are undoubtedly related to storm horizontal structure; stratiform rain fraction and melting-layer effects may be the cause here as well. In addition, the PR's drop size distribution assumptions and attenuation correction scheme may be a source of uncertainty.

Over land, a TMI overestimate is also found in the Tropics and midlatitude warm seasons, but this disagreement with the PR is likely not due to melting-layer effects because emission channels are not used and melting-layer emission is small at 85 GHz (and would actually act to decrease rain estimates). It is more likely due to simply the inappropriateness of the empirically derived 85-GHz ice scattering-rain relationship in storm types seen in the warm seasons at midlatitudes and in the Tropics, and this effect is shown in the relationships among system-by-system areal, convective-stratiform fraction, cloud height, and convective intensity parameters. McCollum et al. (2002) have shown that the NESDIS ice-scattering portion of the TMI algorithm tends to overestimate relative to gauges over the eastern United States. In the future version 6 of the ice-scattering algorithm, the global estimates will be bias adjusted relative to the PR (McCollum and Ferraro 2003). However, the fundamental variability in cloud systems regionally will leave important regional and seasonal variations in the biases that will need to be addressed.

During the cold seasons in the subtropics, PR estimates generally tended to be closer to or higher than (particularly over land) the TMI and gauge estimates. This result is in agreement with Masunaga et al. (2002), who find that in such regions the PR retrievals of near-surface precipitation water content are higher than those of the TMIs, and McCollum et al. (2002), who find that the NESDIS algorithm used in the TMI tends to underestimate precipitation relative to gauges over the

eastern United States. The fact that the PR is higher than the TMI could again likely be due to the inappropriateness of the ice scattering-rain-rate relationship for land midlatitude systems, an incorrect $Z-R$ relationship for midlatitude rainfall, or an erroneous attenuation correction for intense midlatitude convection.

Other factors that have been shown to affect the TMI rain estimates are beam filling, sensitivity, and coastline and cold surface artifacts—the former two leading to $PR > TMI$, the latter leading to $TMI > PR$. For small precipitation features (small WI, NI), the TMI consistently underestimated with respect to the PR, because of TMI's large footprints (especially over ocean) and a lack of sensitivity (especially over land in shallow rain). Cold surface and coastline artifacts over land, despite improvements from version 4 (Kummerow et al. 2001), still cause artificially high rain rates in the version-5 TMI algorithm.

The implications of these results speak to several points that should be considered in future study, validation, and rainfall algorithm development. The first and most important result is that it has been shown that the rainfall estimate biases must be evaluated as a function of rainfall regime on a regional and seasonal basis. Simply integrating the biases on a zonal basis hides many of the disagreements between algorithms and also hides useful information that can yield insights into the causes of the disagreements. With the reprocessing of the “version 6” TRMM algorithms planned for 2004, a coincident production of a 1997–present PF database will yield a powerful tool to investigate further these regional and seasonal biases. This study shows that a storm by storm approach can elucidate some of the physical processes causing the differences. However, more detailed validation on a regional and storm-by-storm basis is necessary to indicate further algorithm deficiencies.

This study has shown that rainfall biases are a function of storm type over both land and ocean. Because there are characteristic differences in the structures, radiative signatures, and biases by feature type, this information might be used to construct a “smarter” microwave algorithm that uses the physical attributes of an observation to limit its selection of profiles to features in a model database with similar structure and radiative characteristics. To some extent, this can be accomplished by a stratiform-convective separation (which will be included over land in version 6; see McCollum and Ferraro 2003), but further information such as the ice-scattering intensity, horizontal extent, cloud-top height, or other characteristics should be useful in constraining the observed radiances with a proper model simulation that represents the pixel scene more properly. These preliminary results show that more information than just the vector of brightness temperatures seen by the radiometer (PF morphology information, IR cloud top, SST, or even environmental data that relate to the resultant vertical profile of hydrometeors) may be used

to constrain microwave rainfall retrievals better by meteorological “regime.”

The misassignment of rainfall to the improper feature types also has implications for the retrieval of the heating profiles associated with the systems in a given region. The partitioning of rainfall into the proper rainfall regime in a particular location is crucial to assigning properly that regime’s characteristic heating profile (cf. Schumacher et al. 2004). In this study, the high positive bias of the TMI* with respect to the PR for MCSs and WI and the negative bias for NI cause a shift of the rainfall budget in a given region toward MCSs and WI, and thus the retrieved latent heating estimate would be biased toward those types of systems and away from warm rain features. This issue not only has implications for rainfall biases but also for the heating profile biases that are caused. Future satellite validation efforts must produce a coincident product that can be quantitatively compared with the satellite algorithms and placed in the proper context of the satellite dataset. Such a product will aid in better characterizing the bias characteristics of observed precipitation features. Satellite validation efforts from the planned Global Precipitation Mission must focus on creating datasets that can more directly and quantitatively be compared with the satellite observations and can be able to validate more directly the assumptions of the algorithms. For the PR, this should include a wider validation of the crucial DSD assumption and attenuation correction methods. For the TMI, techniques to constrain observed parameter space of hydrometeor phases, mixing ratios, size distributions, and densities must done in the liquid, mixed-phase, and ice regions, not only to improve the retrievals but also the cloud models that simulate them. Some of this information may be gleaned from existing datasets, but more quantitative observational comparisons must be developed for our conceptual and numerical models to be improved in representing the water budgets of precipitating systems.

Acknowledgments. TRMM is a project cosponsored by NASA and NASDA, the Japanese space agency. The authors thank Ramesh Kakar for his continued support of TRMM science. Thanks are given to Jay Mace, Steve Krueger, Julia Paegle, Wes Berg, Bob Meneghini, Tim Lang, Rob Cifelli, Steve Rutledge, Galdino Mota, and Haiyan Jiang for discussions and feedback. Thanks also are given to the three anonymous reviewers, who provided very constructive comments that greatly enhanced this study. We thank Baixe Xi for her valuable data processing assistance. Special thanks are given to Erich Stocker and John Kwiatkowski and the rest of the TRMM Science Data and Information System (TDSIS) at the NASA Goddard Space Flight Center in Greenbelt, Maryland, for providing the TRMM data used in this study. Many have contributed to the development of the PF algorithm in addition to SWN and EJZ, including Dan Cecil, Rick Toracinta, David B. Wolff, and Chris

West. Gauge data were provided by the Global Precipitation Climatology Centre, Offenbach am Main, Germany, (a component of the Global Precipitation Climatology Project, Global Energy and Water Cycle Experiment, World Climate Research Program) through their Web site (available online at <http://www.dwd.de/research/gpcc/>). Wentz et al. (2000) TMI SST data are produced by Remote Sensing Systems and are sponsored by NASA’s Earth Science Information Partnerships (ESIP; a federation of information sites for earth science) and by NASA’s TRMM Science Team (data are available online at <http://www.ssmi.com/>). This research was supported by NASA TRMM Science Grants NAG5-9717 and NAG5-10682; SWN was supported by the NASA Earth System Science Graduate Fellowship Grant NGT5-30423.

REFERENCES

- Adler, R. F., G. J. Huffman, D. T. Bolvin, S. Curtis, and E. J. Nelkin, 2000: Tropical rainfall distributions determined using TRMM combined with other satellite and rain gauge information. *J. Appl. Meteor.*, **39**, 2007–2023.
- Atlas, D., and C. W. Ulbrich, 2002: On the separation of tropical convective and stratiform rains. *J. Appl. Meteor.*, **41**, 188–195.
- , C. W. Ulbrich, F. D. Marks Jr., E. Amitai, and C. R. Williams, 1999: Systematic variation of drop size and radar–rainfall relation. *J. Geophys. Res.*, **104**, 6155–6169.
- Bauer, P., J. P. V. Poiras Baptista, and M. de Iulius, 1999: The effect of the melting layer on the microwave emission of clouds over the ocean. *J. Atmos. Sci.*, **56**, 852–867.
- Berg, W., C. Kummerow, and C. A. Morales, 2002: Differences between east and west Pacific rainfall systems. *J. Climate*, **15**, 3659–3672.
- Ferraro, R. R., 1997: Special Sensor Microwave Imager-derived global rainfall estimates for climatological applications. *J. Geophys. Res.*, **102**, 16 715–16 735.
- , and G. F. Marks, 1995: The development of SSM/I rain-rate retrieval algorithms using ground-based radar measurements. *J. Atmos. Oceanic Technol.*, **12**, 755–770.
- , E. A. Smith, W. Berg, and G. J. Huffman, 1998: A screening methodology for passive microwave precipitation retrieval algorithms. *J. Atmos. Sci.*, **55**, 1583–1600.
- Fiorino, S. T., 2002: Investigation of microphysical assumptions in TRMM radiometer’s rain profile algorithm using KWAJEX satellite, aircraft, and surface datasets. Ph.D. dissertation, The Florida State University, 128 pp.
- Grody, N. C., 1991: Classification of snow cover and precipitation using the Special Sensor Microwave Imager. *J. Geophys. Res.*, **96**, 7423–7435.
- Ha, E., and G. R. North, 1995: Model studies of the beam-filling error for rain-rate retrieval with microwave radiometers. *J. Atmos. Oceanic Technol.*, **12**, 268–281.
- Harris, G. N., Jr., K. P. Bowman, and D.-B. Shin, 2000: Comparison of freezing-level altitudes from the NCEP reanalysis with TRMM precipitation radar brightband data. *J. Climate*, **13**, 4137–4148.
- Hong, Y., J. L. Haferman, W. S. Olson, and C. D. Kummerow, 2000: Microwave brightness temperatures from tilted convective systems. *J. Appl. Meteor.*, **39**, 983–998.
- Houze, R. A., 1993: *Cloud Dynamics*. Academic Press, 573 pp.
- Iguchi, T., and R. Meneghini, 1994: Intercomparison of single-frequency methods for retrieving a vertical rain profile from airborne or spaceborne radar data. *J. Atmos. Oceanic Technol.*, **11**, 1507–1517.
- , T. Kozu, R. Meneghini, J. Awaka, and K. Okamoto, 2000:

- Rain-profiling algorithm for the TRMM precipitation radar. *J. Appl. Meteor.*, **39**, 2038–2052.
- Jameson, A. R., and A. B. Kostinski, 2002: Spurious power-law relations among rainfall and radar parameters. *Quart. J. Roy. Meteor. Soc.*, **128**, 2045–2058.
- Kozu, T., and Coauthors, 2001: Development of precipitation radar onboard the Tropical Rainfall Measuring Mission (TRMM) satellite. *IEEE Trans. Geosci. Remote Sens.*, **39**, 102–116.
- Kummerow, C. D., W. S. Olson, and L. Giglio, 1996: A simplified scheme for obtaining precipitation and vertical hydrometeor profiles from passive microwave. *IEEE Trans. Geosci. Remote Sens.*, **34**, 1213–1232.
- , W. Barnes, T. Kozu, J. Shiue, and J. Simpson, 1998: The Tropical Rainfall Measuring Mission (TRMM) sensor package. *J. Atmos. Oceanic Technol.*, **15**, 809–817.
- , and Coauthors, 2001: The evolution of the Goddard profiling algorithm (GPROF) for rainfall estimation from passive microwave sensors. *J. Appl. Meteor.*, **40**, 1801–1820.
- Legates, D. R., and C. J. Willmott, 1990: Mean seasonal and spatial variability in gauge corrected, global precipitation. *Int. J. Climatol.*, **10**, 111–127.
- Masunaga, H., T. Iguchi, R. Oki, and M. Kachi, 2002: Comparison of rainfall products derived from TRMM microwave imager and precipitation radar. *J. Appl. Meteor.*, **41**, 849–862.
- McCollum, J. R., and R. R. Ferraro, 2003: The next generation of NOAA/NESDIS TMI, SSM/I, and AMSR-E microwave land rainfall algorithms. *J. Geophys. Res.*, **108**, 8382, doi:10.1029/2001JD001512.
- , A. Gruber, and M. B. Ba, 2000: Discrepancy between gauges and satellite estimates of rainfall in equatorial Africa. *J. Appl. Meteor.*, **39**, 666–679.
- , W. F. Krajewski, R. R. Ferraro, and M. B. Ba, 2002: Evaluation of biases of satellite rainfall estimation algorithms over the continental United States. *J. Appl. Meteor.*, **41**, 1065–1080.
- Mohr, K. I., and E. J. Zipser, 1996: Mesoscale convective systems defined by their 85-GHz ice scattering signature: Size and intensity comparison over tropical oceans and continents. *Mon. Wea. Rev.*, **124**, 2417–2437.
- Mota, G. V., 2003: Characteristics of rainfall and precipitation features defined by the Tropical Rainfall Measuring Mission over South America. Ph.D. dissertation, University of Utah, 215 pp.
- Mugnai, A., H. J. Cooper, E. A. Smith, and G. J. Tripoli, 1990: Simulation of microwave brightness temperatures of an evolving hailstorm at SSM/I frequencies. *Bull. Amer. Meteor. Soc.*, **71**, 2–13.
- Nesbitt, S. W., E. J. Zipser, and D. J. Cecil, 2000: A census of precipitation features in the Tropics using TRMM: Radar, ice scattering, and lightning observations. *J. Climate*, **13**, 4087–4106.
- Nicholson, S. E., and Coauthors, 2003a: Validation of TRMM and other rainfall estimates with a high-density gauge dataset for West Africa. Part I: Validation of GPCC rainfall product and pre-TRMM satellite and blended products. *J. Appl. Meteor.*, **42**, 1337–1354.
- , and Coauthors, 2003b: Validation of TRMM and other rainfall estimates with a high-density gauge dataset for West Africa. Part II: Validation of TRMM rainfall products. *J. Appl. Meteor.*, **42**, 1355–1368.
- Olson, W. S., P. Bauer, C. D. Kummerow, Y. Hong, and W.-K. Tao, 2001: A melting-layer model for passive/active microwave remote sensing applications. Part II: Simulation of TRMM observations. *J. Appl. Meteor.*, **40**, 1164–1179.
- Petersen, W. A., and S. A. Rutledge, 2001: Regional variability in tropical convection: Observations from TRMM. *J. Climate*, **14**, 3566–3586.
- Prabhakara, C., G. Dalu, G. L. Liberti, J. J. Nucciarone, and R. Suhasini, 1992: Rainfall estimation over oceans from SMMR and SSM/I microwave data. *J. Appl. Meteor.*, **31**, 532–552.
- Rickenbach, T. M., and S. A. Rutledge, 1998: Convection in TOGA COARE: Horizontal scale, morphology, and rainfall production. *J. Atmos. Sci.*, **55**, 2715–2729.
- Rudolf, B., 1993: Management and analysis of precipitation data on a routine basis. *Proc. Int. WMO/IAHS/ETH Symp. Precipitation and Evaporation*, Bratislava, Slovakia, Slovak Hydrometeorology Institution, 69–76.
- , H. Hauschild, W. Reuth, and U. Schneider, 1994: Terrestrial precipitation analysis: Operational method and required density of point measurements. *Global Precipitations and Climate Change*, M. Desbois and F. Desalmond, Eds., NATO ASI Series 1, Vol. 26, Springer-Verlag, 173–186.
- Schumacher, C., and R. A. Houze Jr., 2003: Stratiform rain in the Tropics as seen by the TRMM precipitation radar. *J. Climate*, **16**, 1739–1756.
- , —, and I. Kraucunas, 2004: The tropical dynamical response to latent heating estimates derived from the TRMM precipitation radar. *J. Atmos. Sci.*, **61**, 1341–1358.
- Serra, Y. L., and M. J. McPhaden, 2003: Multiple time- and space-scale comparisons of ATLAS buoy rain gauge measurements with TRMM satellite precipitation measurements. *J. Appl. Meteor.*, **42**, 1045–1059.
- Short, D. A., and K. Nakamura, 2000: TRMM radar observations of shallow precipitation over the tropical oceans. *J. Climate*, **23**, 4107–4124.
- Simpson, J., R. F. Adler, and G. R. North, 1988: A proposed Tropical Rainfall Measuring Mission (TRMM) satellite. *Bull. Amer. Meteor. Soc.*, **69**, 278–295.
- Spencer, R. W., H. M. Goodman, and R. E. Hood, 1989: Precipitation retrieval over land and ocean with the SSM/I: Identification and characteristics of the scattering signal. *J. Atmos. Oceanic Technol.*, **6**, 254–273.
- Tustison, B., D. Harris, and E. Foufoula-Georgiou, 2001: Scale issues in verification of precipitation forecasts. *J. Geophys. Res.*, **106**, 11 775–11 784.
- Vivekanandan, J., J. Turk, and V. N. Bringi, 1991: Ice water path estimation and characterization using passive microwave radiometry. *J. Appl. Meteor.*, **30**, 1407–1421.
- Wentz, F. J., C. Gentemann, D. Smith, and D. Chelton, 2000: Satellite measurements of sea-surface temperature through clouds. *Science*, **288**, 847–850.
- Wilheit, T. T., A. T. C. Chang, M. S. V. Rao, E. B. Rodgers, and J. S. Theon, 1977: Satellite technique for quantitatively mapping rainfall rates over oceans. *J. Appl. Meteor.*, **16**, 551–560.
- , —, and L. Chiu, 1991: Retrieval of monthly rainfall indices from microwave radiometric measurements using probability distribution functions. *J. Atmos. Oceanic Technol.*, **8**, 118–136.
- Xie, P., and P. A. Arkin, 1995: An intercomparison of gauge observations and satellite estimates of monthly precipitation. *J. Appl. Meteor.*, **34**, 1143–1160.
- Zipser, E. J., 1982: Use of a conceptual model of the life cycle of mesoscale convective systems to improve very short range forecasts. *Nowcasting*, K. Browning, Ed., Academic Press, 191–204.